



Formation of highly resistive SiO₂ nanoparticle layers from the aerosol by electrostatic precipitation at 200 °C: observations on back corona and nanoparticle layer structure

Patrick Bürger · Ulrich Riebel

Received: 21 January 2021 / Accepted: 19 July 2021 / Published online: 7 August 2021 / Published online: 7 August 2021
© The Author(s) 2021

Abstract In this study, a flame-generated nm-range SiO₂ aerosol (approx. 170 nm median aggregate diameter) is fed into an electrostatic precipitator with an operating temperature of 200 °C. While a highly porous layer of SiO₂ nanoparticles (NPs) is deposited by electrostatic precipitation, a decrease of current uptake is observed initially, indicating exceptionally high values of the electric field within the layer (>100 kV/mm) and of the layer resistivity (>10¹³ Ω·cm). Later a strong (13- to 17-fold) increase of current uptake is observed. Aerosol charge measurements show that charges of opposite polarity are emitted from the NP layer. Investigation of the NP layer by SEM shows that charge-emitting structures with a polarity-dependent morphology develop on an originally homogeneous NP layer. Based on the experimental evidence, the mechanisms of charge emission and structure formation are discussed. Charge emission from the precipitated dust layer is known as back corona in the field of electrostatic precipitation. It appears that the mechanisms of

back corona observed with SiO₂ NP layers are quite distinct from those observed with μm-range particles. While gas discharges inside the NP layer are suppressed due to small pore size, back corona inside the NP layers is apparently initiated by thermionic field emission of free electrons and secondary electron multiplication within the NP layer.

Keywords SiO₂ aerosol · Nanoparticle layers · Highly resistive dust · Back corona · Electrostatic precipitation · Thermionic field emission

Introduction

In the electrostatic precipitation of highly resistive dusts, the so-called back corona (BC) is a common disturbance. Typically, BC is observed with dusts having a resistivity in excess of 10¹⁰ to 10¹¹ Ω·cm (White 1963, 1974; Robinson 1971). BC typically leads to a lowering of spark-over voltage, to an increase of current uptake (for a given value of operating voltage) or even to a reduction of operating voltage (when maintaining a given current uptake). Generally, the efficiency of particle retention is reduced by BC more or less dramatically, depending on operation time (Chang and Bai 1999). The current–voltage characteristic (CVC) can show a hysteresis behavior (Bacchiaga et al. 2006).

Following White (1963), a reduction of current uptake is observed in the initial phase of deposition

P. Bürger · U. Riebel
Lehrstuhl Mechanische Verfahrenstechnik (MVT),
Brandenburgische Technische Universität Cottbus-
Senftenberg (BTU), 03013 Cottbus, Germany

U. Riebel (✉)
Department of Particle Technology, Brandenburg
University of Technology Cottbus-Senftenberg (BTU),
03013 Cottbus, Germany
e-mail: riebel@b-tu.de

of highly resistive dust. When the electric field inside the dust deposit surpasses the dielectric strength of the dust, a dielectric breakthrough occurs and BC is initiated. Simm (1959) reports critical fields in the range of 2 to 4.1 kV/mm and observes that the onset of BC is polarity dependent. White (1974) has recorded breakdown field strengths in the range of 0.8 to 4 kV/mm; however, the values for dust containing conductive particles (high carbon ash) are much lower and amount to 0.1–0.2 kV/mm only.

Authors generally agree that BC is associated with the emission of counter-ions (ions of opposite polarity) from the collection electrode. In most cases, the counter-ions are observed to originate from craters in the dust layer on the collection electrode, whereby the formation of a luminous corona discharge or streamer localized in the crater can be observed (White 1974; Robinson 1971; Ni et al. 2016; Majid et al. 2011). Majid et al. (2011) have visualized the blow-out of dust particles from a crater. In some cases, BC is observed to originate from extended elliptical patches with a reduced thickness of dust (Hoferer and Schwab 2000), or a luminous discharge may appear to cover the dust surface more or less homogeneously (Masuda et al. 1995). Ni et al. (2016) state that the BC appears first in places where the dust thickness is the highest.

In model experiments, the appearance of BC can be mimicked when the collection electrode is covered by a dielectric layer with one or several pinholes or with some porosity (White 1963; Robinson 1971). Jánský et al. (2014a, b) provide detailed numerical simulations on the pinhole discharge, giving insight into different modes of discharge and their dynamics.

The modeling of BC has remained a challenge so far. Lawless and Sparks (1980) present a model on the current–voltage behavior during BC with varying proportions between corona and BC current. The model is able to predict hysteresis behavior. Chang and Bai (1999) show that measurements of grade efficiency can be reproduced with a BC model.

Very little is known so far about the electric properties of highly resistive dust layers. Aleksin et al. (2016) have shown that highly resistive dust layers can be understood as electret materials with the current transport occurring by injected holes and electrons. Furthermore, very strong breakthrough field strengths going up to 80 kV/cm were found in the

case of fine dusts with average particle diameters of a few μm .

The results presented here were found during experiments aiming at the combination of aerosol removal with heat and mass transfer across the collection electrode of an electrostatic precipitator (ESP). A flame-generated SiO_2 nanoparticle aerosol was treated at 200 °C in a wire-tube ESP configuration. The first experiments showed an extremely strong, unexpected rise of the current uptake after some time of operation. A continuous drift of the results was observed when the experiments were repeated. The drift of results can probably be attributed in part to an incomplete removal of the SiO_2 NP layers during cleaning, in part to the formation of hot spots in the NP layer, which cause irreversible changes of the stainless steel surfaces by sintering of SiO_2 . Unfortunately, this restricted the possibility to repeat results, as this would have required new equipment for each single run.

Experimental setup and methods

Experimental setup

The experimental setup consists of the aerosol generator and the laboratory ESP including all necessary peripheral devices to ensure operation and conduct measurements.

The laboratory ESP and its periphery are made of stainless steel piping with pull ring connected flanges. Figure 1 shows a simplified schematic description of the ESP and the exhaust section.

The collection electrode has a diameter of 80 mm, a length of 1030 mm, and an area of 0.259 m^2 . At the lower end of the collection electrode, samples of metal foil are fixed at the tube wall and exposed to the NPs being deposited from the aerosol. Later, these samples are investigated by SEM. Top and bottom sections with a wider diameter (150 mm and 250 mm, respectively) are connected to the collection electrode by cone pieces. The stainless steel discharge wire (diameter of 0.3 mm, total length 1580 mm) is suspended from a ceramic insulator and is subjected to tension by a weight. The weight is guided in a ceramic tube. Insulating blankets made of calcium magnesium silicate fiber are wrapped around the

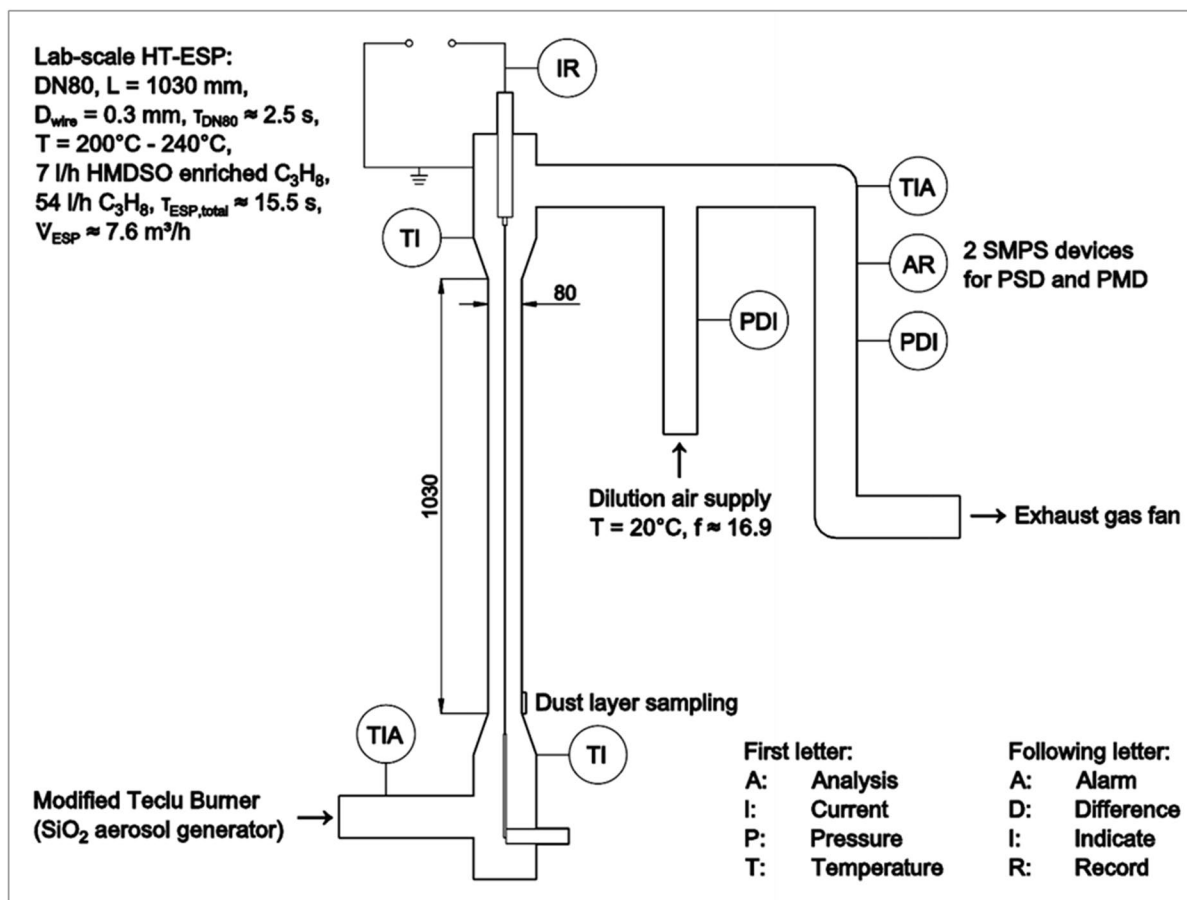


Fig. 1 Simplified schematic description of the lab-scale HT-ESP in wire-tube geometry, with a main collection electrode diameter of 80 mm and 1030 mm length ($Re \approx 870$), a wire diameter of 0.3 mm, and an operating temperature of 200–240 °C

piping to reduce temperature losses in the bottom, ESP, and top sections.

The volume flow of hot SiO₂ aerosol (7.6 m³/h at 200 °C) from the aerosol generator is introduced into the bottom section. The hot residual aerosol leaving from the top section is diluted with ambient air. The flows of the dilution air and of the diluted mixture are measured by orifice plates. The dilution air is admitted with a volume flow of 75 m³/h at 20 °C, giving a 16.9-fold volumetric dilution factor.

A high voltage (HV) power supply with reversible polarity (Heinzinger PNC 30,000 V 20 mA) is used in this study. The current is measured with a resolution of 1 μA using a custom-built device located between the HV source and the discharge electrode. The measured values are transmitted to a personal computer (PC) via optical fiber.

Temperature is measured continuously directly above the burner flame (with a thermocouple type K) and after the dilution of the flow from the ESP by a PT-1000 sensor. Additionally, the gas temperature is measured with thermocouples placed in the entrance to and in the exit from the 80-mm-diameter precipitation section. However, these measurements are only possible while the high voltage is switched off.

Aerosol samples (raw gas, clean gas) for the measurement of the particle size distribution (PSD) and the particle mobility distribution (PMD) are extracted from the diluted exhaust gas.

The aerosol is characterized by the PSD and the PMD, which are measured simultaneously by two SMPS (scanning mobility particle sizer) systems (Grimm model 5.416). PSD and PMD results are shown as-diluted, without a correction.

The SMPS used for measuring the PSD is equipped with an x-ray aerosol neutralizer (TSI model 3088) adapted to the Grimm system. The measurement range is from 10 to 1055 nm particle diameter. The particle number concentration determined with the SMPS system is the total number concentration (TNC) C_N , including electrically neutral particles.

For the measurement of the PMD, the second SMPS is customized with a reversible DMA voltage supply and operated in the “raw count mode” without aerosol neutralization. This means only those particles are measured and indicated which bear an electrical charge with a polarity opposite to the DMA polarity. There is no assumption of any kind on particle charge distribution, and neutral particles are not included in the raw count number concentration $C_{N,RC}$. A special feature of the raw count mode is that it can be used for the detection of inversely charged particles (ICPs). For the measurement of ICPs, the DMA polarity is set identical to the discharge polarity of the ESP wire. The appearance of ICPs is an excellent, unmistakable indicator for BC effects.

Aerosol generator and aerosol characteristics

The nm-range SiO_2 aerosol is produced by combustion of hexamethyldisiloxane (HMDSO) in a gas burner. For this, a Teclu burner is modified by adding a capillary tube which allows introducing a gaseous propane/HMDSO mixture directly into the base of the flame.

The overall propane flow to the burner is kept constant at 54 l/h which corresponds to 1.4 kW. A part of the propane flow (7 l/h) is branched off and is saturated with HMDSO at 19 °C. The aerosol generator provides a reliable and reproducible aerosol in respect to the PSD and the TNC. With the vapor pressure of HMDSO amounting to 4300 Pa at 20 °C (IFA 2019), the production rate of SiO_2 is near 160 mg/h. The PSD and the charging state of the raw gas particles are determined by sampling from the exhaust pipe while the ESP high voltage was switched off.

Generally, flame-generated aerosols are subjected to very high temperatures and to a high concentration of ions during their production. Hence, we may expect that the aerosol particles initially show a bipolar charge distribution corresponding to the flame temperature. Additionally, the high temperatures promote the formation of sintering necks between

coagulated primary particles, forming aggregates in the process (Seipenbusch et al. 2010). Figure 2a shows the PSD of the raw gas aerosol for TRE #5 and TRE #6 as an example. The diluted TNC of the raw gas in these experiments was $9.3 \cdot 10^6 \text{ cm}^{-3}$ and $8.9 \cdot 10^6 \text{ cm}^{-3}$, respectively. Based on the dilution factor, the TNC at the inlet of the ESP is estimated to be around $1.54 \cdot 10^8 \text{ cm}^{-3}$. The median number diameter of the raw gas NPs during these experiments was 173 nm and 168 nm, respectively.

In addition, Fig. 2b gives the raw counts for the original aerosol and, in comparison, the aerosol neutralized at ambient temperature by the x-ray neutralizer. We see that the TNC shown in Fig. 2a is much higher than the number of raw counts, because in equilibrium, only a fraction of the aerosol particles is charged.

In the original aerosol from the flame generator, the number of raw counts is significantly higher, because the charge distribution of the particles formed at flame temperature is frozen at some point when the flame aerosol mixes with the surrounding stream of cold air. The close coincidence of positive and negative raw count mobility distributions shows that the original aerosol is almost neutral.

Time-response experiments-execution and results

In the electrostatic precipitation of dry solid dusts, a steady state cannot be reached, because the build-up of the dust cake acts back on the electrostatic discharge. Therefore, the precipitation of the SiO_2 NPs and the development of BC were studied in time-response experiments (TREs). In these experiments, only the starting conditions and some of the input data are constant or nearly constant, while other data like current uptake, precipitation efficiency, and BC are developing with time. Details of the experimental settings and the methodology of the TREs can be found in the Appendix. Before each TRE, the plant was cleaned thoroughly according to the regimen described in the Appendix.

Table 1 summarizes key data for the different TREs such as initial current, final current, total number concentration of raw gas and final clean gas, and the separation efficiency reached at the end of the experiments.

Fig. 2 a Particle size distribution (PSD) of the diluted SiO₂ aerosol used in the time-response experiments (TREs) (above). **b** Simultaneously measured particle mobility distribution (PMD) with and without aerosol neutralization (AN) of the diluted SiO₂ aerosol (below)

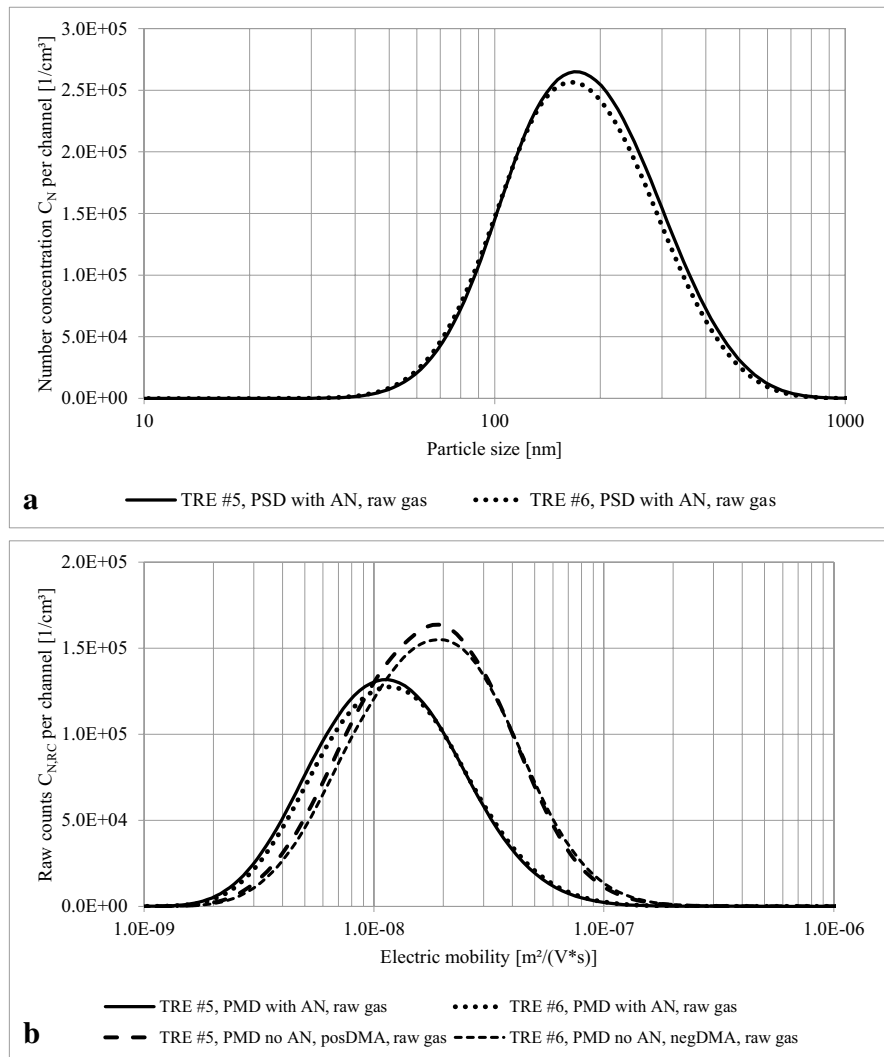


Table 1 Overview of time-response experiments (TREs) regarding ESP discharge polarity, operating voltage (*U*), blank and final current (*I*), total number concentration (*C_N*) of raw gas and clean gas (*f* ≈ 16.9), and final separation efficiency (*η_{final}*). TRE #7 was aborted after 50 min due to multiple spark-over events

Measurement	<i>U</i>	<i>I_{blank}</i>	<i>I_{final, aerosol}</i>	<i>C_{N, raw gas}</i>	<i>C_{N, clean gas, final}</i>	<i>η_{final}</i>
TRE #1	+ 10 kV	0.446 mA	5.55 mA	9.64•10 ⁶ cm ⁻³	7.48•10 ⁶ cm ⁻³	22%
TRE #2	- 10 kV	0.811 mA	8.25 mA	9.98•10 ⁶ cm ⁻³	6.39•10 ⁶ cm ⁻³	36%
TRE #3	- 10 kV	0.890 mA	8.13 mA	10.28•10 ⁶ cm ⁻³	7.85•10 ⁶ cm ⁻³	24%
TRE #4	+ 10 kV	0.482 mA	5.74 mA	9.50•10 ⁶ cm ⁻³	6.88•10 ⁶ cm ⁻³	28%
TRE #5	+ 10 kV	0.437 mA	5.88 mA	9.29•10 ⁶ cm ⁻³	5.91•10 ⁶ cm ⁻³	36%
TRE #6	- 10 kV	1.318 mA	12.69 mA	8.93•10 ⁶ cm ⁻³	5.81•10 ⁶ cm ⁻³	35%
TRE #7, aborted	+ 10 kV	0.606 mA	6.03 mA	8.77•10 ⁶ cm ⁻³	5.11•10 ⁶ cm ⁻³	42%

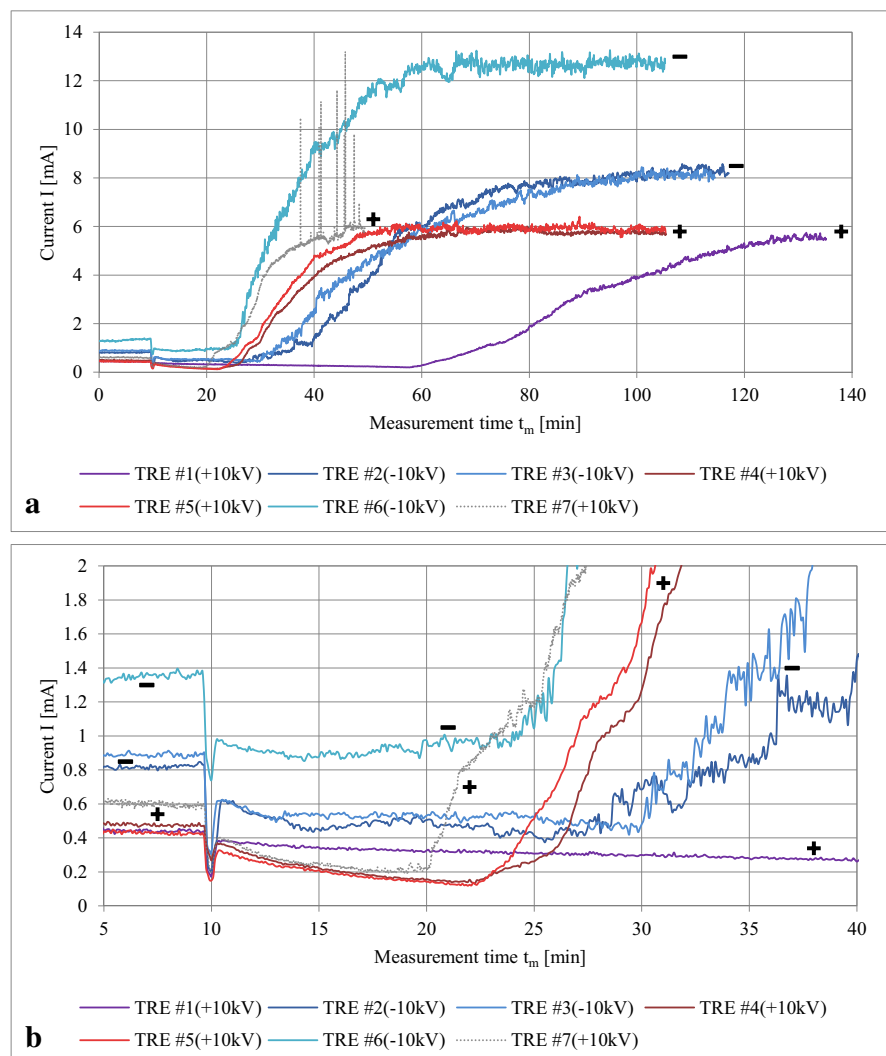
Electric current uptake

The current for all TREs is shown in Fig. 3. During the first 10 min of measurement time (t_m), a constant current uptake is found in the absence of aerosol. When the SiO₂ aerosol is admitted at $t_m=10$ min, the current uptake drops sharply and recovers partially within several seconds, when a near-stationary regime is established. The mechanism of this initial current drop is “corona quenching,” caused by the space charge of the aerosol (Lübbert 2011). While the overall space charge is limited, much of the ion charge is transferred to aerosol particles which have a much lower mobility. Hence, the average mobility of the charge carriers and the current uptake are

reduced. It appears that the corona quenching effect is significantly stronger with the negative corona, which might be seen as an indication for the presence of some charging by free electrons (Bürger and Riebel 2020).

After the admission of the aerosol, we observe a “low current phase.” The low current phase continues for a more or less extended period of time. In detail (see Fig. 3b), the current uptake always falls off gently for a variable period of 5 to 25 min. The “falling current” phase is visible especially for the runs with positive corona (TRE #4, TRE #5, TRE #7). The very first experiment executed with a brand-new collection electrode (TRE #1) stands out with the “falling current” phase lasting for about 50 min and a different

Fig. 3 **a** Current uptake for all time-response experiments (TREs). SiO₂ aerosol is admitted at 10 min, when the initial temperature has been reached (200–210 °C). **b** Enlarged detail showing current uptake during the low current phase and the early transition phase



slope. In case of positive polarity, the falling current phase ends quite abruptly, when the current uptake starts to rise. In case of negative corona (TRE #2, TRE #3, TRE #6), the “falling current” phase lasts only for about 5 min and is followed by a phase of constant current uptake which is superimposed by relatively strong fluctuations.

In a first qualitative interpretation of the “falling current” phase, this effect is ascribed to the formation of a thin, homogeneous layer of NPs on the collection electrode. As the NP material (SiO_2) is highly resistive, a significant potential difference is needed to drive the discharge current through the NP layer. With increasing NP layer thickness, the net potential difference which is left for maintaining the corona discharge is increasingly reduced and the current uptake will decrease accordingly. Later (and mostly with negative corona polarity), the falling current effect appears to be superimposed by other effects. We may speculate that initial stages of BC are developing already early during the low current phase, or that the corona onset voltage is shifted to lower values by increasing roughness of the corona wire due to the deposition of NPs. Indeed, significant deposits of NPs (about 0.5 mm in thickness) are found on the corona wire when the wire is cleaned at the end of each TRE (after the CVCs have been measured). With negative corona the deposit is smooth, while with positive corona some dendritic structures are found.

At the end of the low current phase, we always observe a transition phase. During the transition phase, the current rises much (13- to 17-fold) above the low current level measured shortly after the admission of aerosol, and even much (9- to 13-fold) above the current (I_{blank}) measured before the aerosol is admitted. After some time, the high current phase with a more or less stable level of current uptake is reached. It appears that all four of the TRE runs with positive corona end with the same high-level current. The first two TREs with negative corona (TRE #2 and TRE #3) also show good agreement. The last two TREs probably are atypical results. TRE #6 started with a significantly higher initial current and ended with a higher BC current. TRE #7 started with a higher current level than the other runs with positive polarity and had to be aborted early because of sparking.

In a preliminary interpretation, we explain the transition and the high current phase by the formation

of a strong BC. Charges of opposite polarity generated from the NP layer are reducing both particle space charge and ionic space charge, which allows an increase in current at stationary voltage while the space charge limitation is still fulfilled.

On a second view, we find that the duration of the low current phase is not stable but shortens continuously from TRE #1 and TRE #7. Additionally, we see that the current uptake in the initial phase (prior to the admission of aerosol) is not stable either, but also shows a tendency to increase compared to the previous run with the same polarity. Both effects might be seen as an indication for an irreversible change of the experimental conditions. Possibly the applied cleaning regime did not completely remove the SiO_2 dust layer from the collection electrode and/or from the corona wire. Indeed, a revision of the cleaning procedure which was done after the end of the experiments (see Fig. 13) revealed that the NP layer could not be removed completely from the collection electrode.

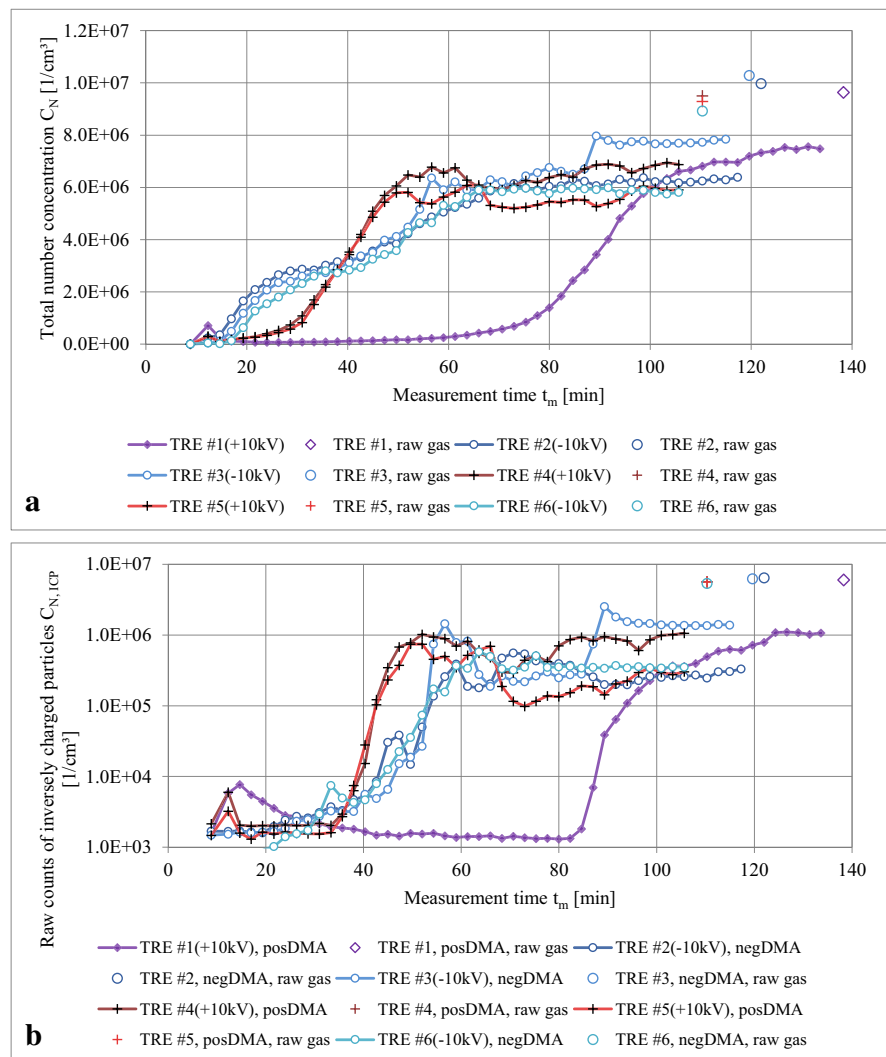
Clean gas aerosol and separation efficiency

More insight into the precipitation process can be gained when the emission of particles with the clean gas is discussed. The separation efficiency is the ratio between the number of particles collected in the apparatus in relation to the number of particles entering with the raw gas:

$$\eta = \frac{C_{\text{N,raw gas}} - C_{\text{N,clean gas}}}{C_{\text{N,raw gas}}} \quad (1)$$

Figure 4a shows the TNC of particles in the diluted clean gas for all seven TRE experiments. The first experiment (TRE #1, \diamond markers) was conducted with positive corona and shows at least 30 min of very low emission until the TNC rises continuously. After a strong increase between 70 and 110 min, the TNC levels out around $7.5 \cdot 10^6 \text{ cm}^{-3}$, which is not far from the TNC in the raw gas ($9.64 \cdot 10^6 \text{ cm}^{-3}$). In fact, the precipitation efficiency drops from 99 to only 22% (see Fig. 5b for separation efficiency plots). Compared to all following experiments, TRE #1 shows a long period of operation with acceptable separation efficiency. Even though the piping was cleaned thoroughly between consecutive TREs to achieve a common starting point, the results from the “brand-new” collection electrode could not be reached again

Fig. 4 a Total number concentration (C_N) in the diluted clean gas for all time-response experiments (TREs) with SiO_2 aerosol addition starting at 10 min and 200–210 °C initial temperature. The single symbols indicate the raw gas C_N as measured in the end of the respective TREs. TREs with positive corona show a later but steeper increase in concentration than experiments with negative corona. **b** Inversely charged particles (ICPs) measured in the diluted clean gas. ICPs in the raw gas were measured in the end of the TREs and are shown as single points. We observe that increases in the ICPs are correlated to increases of clean gas C_N , especially when the ICPs are on a high level



by cleaning. The further runs with positive corona (TRE #4, TRE #5, + markers) can maintain good separation efficiency (>95%) for about 20 min. This coincides with the observations on current decrease during the low current phase which was discussed above.

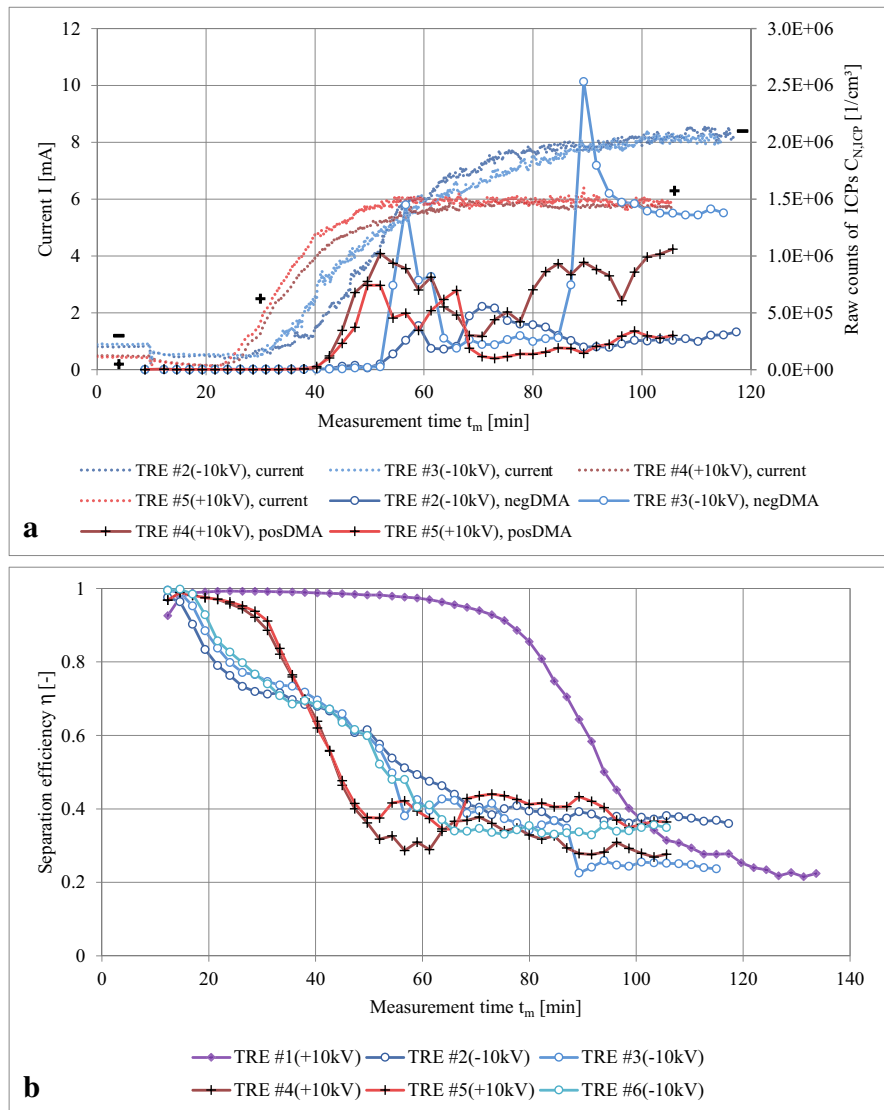
Possibly the initial, slow rise in clean gas particle emission with positive corona simply reflects the growing resistance of the dust layer and the corresponding weakening of corona current and electrostatic field. Both factors slow down particle charging and particle migration to the collection electrode.

The experiments with negative corona (TRE #2, #3, #6, O markers) show a behavior which

is clearly distinct from comparable runs with positive corona (TRE #4, #5). With negative corona, the rise in clean gas particle emission or the loss in separation efficiency, resp., is much stronger right from the beginning. This coincides with a more pronounced decrease of the current uptake in the “falling current” phase. Possibly this indicates that the dust resistivity is polarity dependent and has a higher value for negative corona.

In the final high current phase, the clean gas TNC is comparable between all experiments with both polarities and reaches 65–75% of the raw gas TNC.

Fig. 5 a Raw counts of diluted inversely charged particles (ICPs) as a function of measurement time, together with the current uptake. In some peaks (TRE #3 @ 90 min), the ICP count may amount to about 30% of the clean gas TNC. **b** Number-related separation efficiency η as a function of measurement time. Note the correlation between highs in the ICP emission and lows in the separation efficiency



Inversely charged particles

Simultaneously to the measurements of the TNC, the number of ICPs was measured as explained above. Figure 4b shows the diluted ICP raw counts $C_{N,ICP}$ on a logarithmic scale.

First, we see that the ICPs which are originally contained in the raw gas (around $8 \cdot 10^6 \text{ cm}^{-3}$, single point at $t_m = 120\text{--}140 \text{ min}$) disappear almost completely. Only about $5 \cdot 10^3 \text{ cm}^{-3}$ ICPs survive when the aerosol passes through a clean ESP in the starting phase of the experiments.

Together with the rise of current uptake, the start of BC, and the rise in clean gas TNC, the emission

of ICPs is observed. Early stages of ICP emission are visible only on a logarithmic scale (Fig. 4b). However, ICPs appear with a little delay following the rise in TNC (Fig. 4a). The delay is explained as ICPs will most probably be emitted first in the entrance part of the ESP where the NP layer grows fastest. During their further passage through the ESP, these ICPs can be eliminated by ions from the corona or by electrostatically enhanced agglomeration.

Again, it appears that the ICPs behave quite distinctly with positive and negative corona. With positive polarity (TRE #1, TRE #4, TRE #5), the ICPs stay on a low level for a longer time, but then the rise occurs extremely fast. In the case of negative

corona (TRE #2, TRE #3, TRE #6), the ICPs start to rise at $t_m=20$ min already, about 10 min before the current uptake starts to rise visibly. For both corona polarities, significant amounts of ICPs (more than 10^4 cm^{-3}) are found in the clean gas only after the current has reached about 60% of its final level.

Similar to the TNCs, the number of ICPs reaches a more or less stable value when the current reaches the stationary phase. However, the ICPs show much more pronounced fluctuations during the stationary phase. Relating the number of ICPs to the TNC, we find that in the final state of BC, around 10 to 30% of the clean gas aerosol particles are emitted as ICPs.

Also, we see that the number of ICPs still shows very strong fluctuations when the current uptake has stabilized on the high level. In Fig. 5a, the diluted ICPs are plotted on a linear scale together with the current uptake. It appears that there is no visible correlation between fluctuations of the ICPs and fluctuations of the current uptake, respectively.

On the other hand, Fig. 5b shows the number-related separation efficiency as a function of measurement time. The separation efficiency has the highest values right in the beginning of the experiments and decreases significantly with time. As seen already in the diagrams showing the TNC, experiments with positive corona maintain a better separation efficiency at the beginning while TREs with negative corona show a continuous reduction in separation efficiency from the beginning.

Furthermore, we observe a significant correlation between peaks of the (linearly plotted) ICPs (Fig. 5a) and lows of the separation efficiency (Fig. 5b).

Current–voltage characteristics

The trend of consecutive TREs, showing a decreasing duration of the low current phase, a reduced time until the appearance of ICPs, and an earlier transition to BC, had been observed in earlier experiments already. This observation had led to the suspicion that, in spite of careful cleaning of the ESP section between the single experiments runs, some irreversible changes of the electrodes are taking place during the ESP operation. Therefore, extra measurements of the current–voltage characteristics (CVCs) at 20 °C and at 200 °C were made systematically with the brand-new equipment and after each

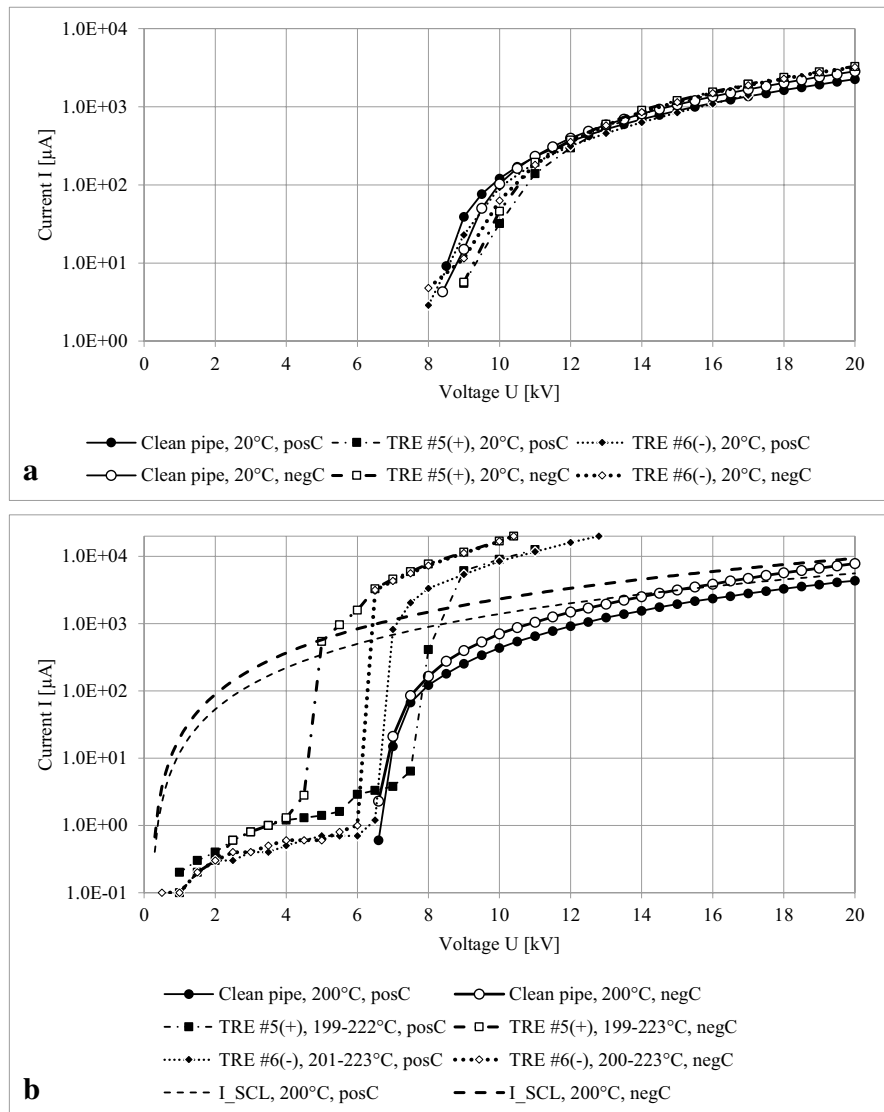
TRE in order to gain more insights into the non-repeatability of the TRE runs.

The 20 °C CVCs (Fig. 6a) are nearly invariant between the brand-new state and the state with NP deposits after the TREs. There is definitely no sign of BC at 20 °C. The near-invariance of the 20 °C CVCs shows that the geometry of the wire-tube arrangement has remained unchanged. The NP deposit on the collection electrode does not have an influence on the CVC, because all hydrophilic dusts (including SiO_2 NPs) adsorb water vapor from the atmosphere and have a low resistivity due to surface conduction (White 1974; Robinson 1971; Majid et al. 2011; Masuda et al. 1995). Typically, the resistivity maximum of dusts in air or flue gas is found in a temperature range between 150 and 300 °C, when humidity, SO_2 , and acid gasses have been desorbed from the surface.

In contrast, strong effects from the deposited SiO_2 NPs are found with the 200 °C CVCs. Figure 6b presents CVCs at 200 °C and includes three different types of curves: (i) positive and negative CVCs measured with the brand-new apparatus which has never been in contact with SiO_2 NPs; (ii) CVCs measured with the dust-laden apparatus after a specific TRE run. For example, “TRE #5(+), 199–223 °C, negC” means that the CVC was measured after completing TRE #5, which was run with a positive corona; however, the CVC was measured afterwards with negative corona. (iii) Positive and negative CVCs which are derived theoretically based on the Monrolin-Praud-Plouraboué (MPP) equation for a corona onset voltage of nearly zero (for reasons of numerical stability, the CVC is calculated with an onset voltage of $U_0=0.2$ kV). The corresponding ion mobilities at 200 °C are extracted from the “brand-new” CVCs using the MPP equation and amount to $3.4 \cdot 10^{-4} \text{ m}^2/(\text{V s})$ for positive corona and $5.65 \cdot 10^{-4} \text{ m}^2/(\text{V s})$ for negative corona (White 1963; Townsend and Edmunds 1914; Monrolin et al. 2018). Hence, these CVCs (named I_{SCL}) represent the maximum current which is possible for a unipolar corona under limitation by space charge.

In the logarithmic representation, we find that the corona onset voltages (slightly above 6.5 kV for both polarities with the brand-new apparatus) are shifted towards lower voltages (4–6 kV), when a negative voltage is applied. For positive corona, the onset voltage is not changed significantly (TRE #6(–), posC),

Fig. 6 Current–voltage characteristics at 20 °C (a) and 200 °C (b) for positive (thin lines) and negative (thick lines) polarity, measured with ascending voltage for clean (brand-new) piping (solid line, ○ markers) and dust layered piping measured after cooldown and reheating: TRE #5 + 10 kV (dotted line, □ markers) and TRE #6 – 10 kV (dotted line, ◇ markers). The curves without symbols (dashed lines) show the space charge limited current (I_{SCL}) assuming a corona onset voltage near zero



or even is shifted towards a slightly higher voltage (TRE #5(+), posC).

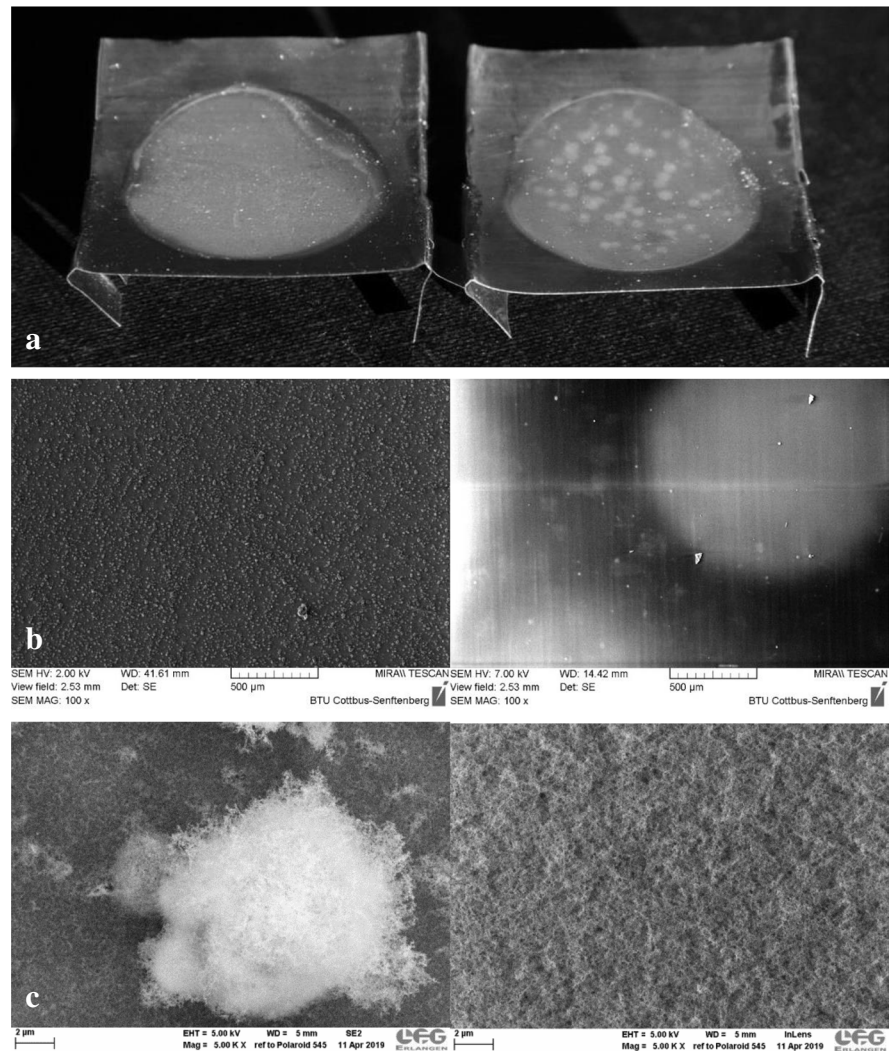
In all cases, the corona current is increased by more than one order of magnitude compared to the reference measurements with the brand-new apparatus, and in all cases, the current is higher than the current limited by unipolar space charge (I_{SCL}). As the current uptake is limited (in the absence of an aerosol) by the ion space charge, and the mobility of the ions should not vary too much, there is only one possible explanation: There must be an emission of positive ions or free electrons producing negative ions from the collection electrode. As these ions are of opposite polarity to the ions produced at the corona

wire, the overall space charge is reduced (for a given current density), or a higher current will be emitted from the corona wire in fulfillment of the space charge condition.

Meanwhile, a new regime of current generation can be found in the range of low currents or voltages, below the corona onset voltage. Current starts to flow through the gas at very low voltage (1 kV and less) already and increases only slightly with increasing voltages. The current remains on a low level, clearly below the space-charge limited current I_{SCL} .

In a preliminary interpretation, we may explain the sub-onset currents by the mechanism of

Fig. 7 SiO₂ dust layer samples from time-response experiments. Left sides: TRE #2 with negative ESP polarity. Right sides: TRE #1 with positive ESP polarity. From top to bottom: **a** Optical image: The transparent dust layers are visualized by back-scattered light. The circular samples are 25 mm in diameter. On the right, freckled structure from positive polarity. **b** SEM, magnification 100×: Uniformly distributed agglomerate-like protrusions deposited by neg. corona (left), and smooth layer deposited by pos. corona (right) with a freckle of higher dust density and with single white spots. **c** SEM, magnification 5000×: Single protrusion from neg. corona (left) and smooth layer from pos. corona (right)



thermionic field emission. The NPs on the corona wire or the collection electrode might act in two different ways: first, as an emitter material with a low work function for electrons, so that emission becomes possible already at low voltages. Second, the deposited NPs might be seen as a dielectric material which nevertheless allows a certain amount of current transport by injected electrons or holes. Possibly the behavior of such materials can resemble to the behavior of conductive particles (Vora et al. 2019). This allows the build-up of high fields which allow either the thermionic field emission of free electrons (on the cathode side only) or the development of microscopic, intermittent gas discharges.

Survey of the SiO₂ dust layer structure using SEM

The dust layer samples are obtained from a 25-mm hole in the wall of the collection electrode. The opening is covered with a thin copper foil. During the TREs, SiO₂ NPs are deposited on the collection electrode and the copper foil. The dust sample is removed after the CVCs have been measured.

In most of the TRE runs, particles are produced and deposited for 100 min. The particle production rate is slightly below 160 mg/h = 267 mg/run. Assuming that the SiO₂ NPs have a material density of 2.2 g/cm³ and deposit uniformly onto the surface of the collection electrode (diameter 80 mm, length 1030 mm, area 0.259 m²), we would expect a NP layer thickness corresponding to about 0.48 μm of massive SiO₂. A

sample with 25 mm diameter should receive a deposit of 0.51 mg. In comparison, the mass of the dust layers shown in Fig. 7a amounts to 0.6 mg (TRE #2, left) and 0.8 mg (TRE #1, right) respectively. The deviations are easily explained, as the samples were taken shortly after the entrance of the aerosol into the precipitator, where the aerosol concentration and the particle deposition rate are still above the average value.

Of course, the dust layers are porous. SEM images (Fig. 8) show that the real thickness of the dust deposits is in the range of 4 μm (neg. corona) to

11 μm (pos. corona). This is the eightfold to 23-fold of the theoretical thickness of a massive SiO₂ layer. As a result, we may estimate the porosity of the layer to be around 95% (pos. corona) based on the measured mass of the dust layer. The thickness of the dust layer deposited by negative corona cannot be used to estimate the porosity due to its complicated structure. The polarity-induced differences of dust layer structure are visualized in Figs. 7, 8, 9, and 10 and will be discussed in the following.

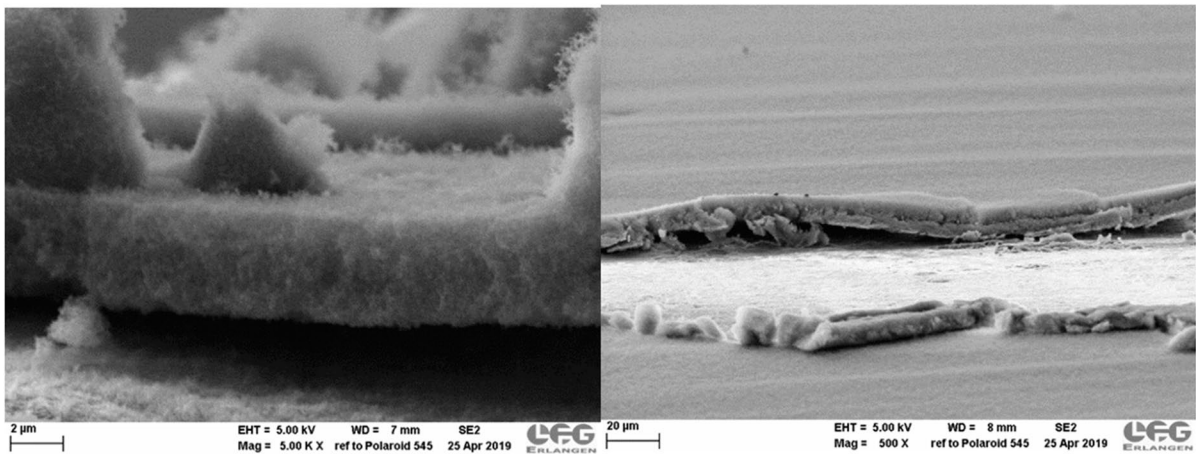


Fig. 8 Lateral SEM image showing the structure and thickness of the dense uniform dust layer with 5000× magnification for TRE #2 with negative ESP polarity (left, 4 μm dust layer)

and 500× magnification for TRE #4 with positive ESP polarity (right, 11 μm dust layer)

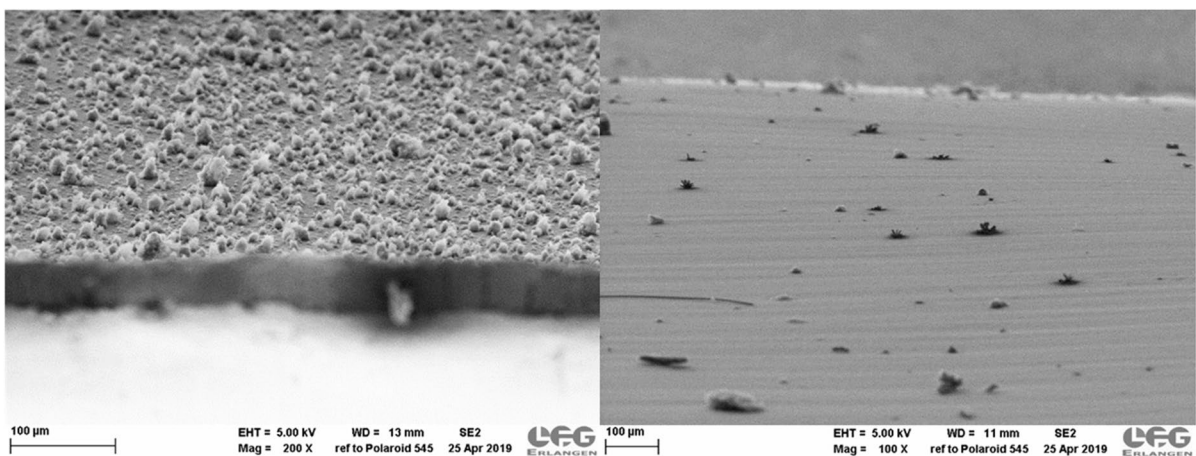


Fig. 9 Lateral SEM image with 200× magnification of SiO₂ dust layer sample for TRE #2 with negative ESP polarity showing uniformly distributed μm-scale agglomerate-like

protrusions (left) and 100× magnification for TRE #4 with positive ESP polarity showing a dense uniform layer and a few dense dendritic structures several 100 μm apart (right)

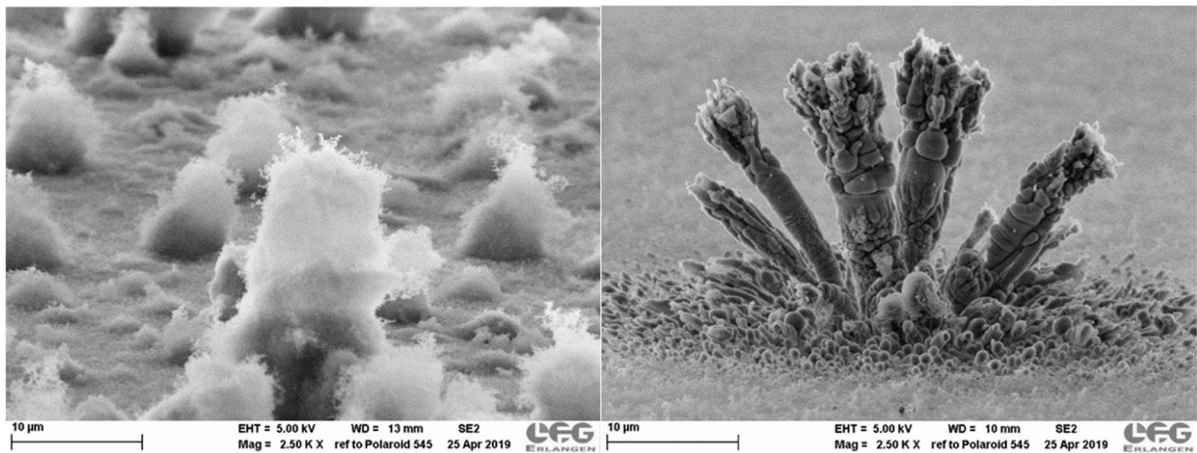


Fig. 10 SEM, lateral view, 2500 \times . Samples from TRE #2 with negative ESP polarity showing μm -scale agglomerate-like protrusions (left) and from TRE #4 with positive ESP polarity showing a very dense dendritic structure (right)

Figure 7a shows optical photographs of two samples (TRE #1 (+10 kV, right hand side) and TRE #2 (−10 kV, left hand side)) with NP deposits of 25 mm diameter. The very thin dust layer is hardly visible due to the nm-range particles and the high porosity of the layer itself. In order to make the dust layers visible, backscattering is produced by pointing a strong source of light onto the samples in a flat angle from behind the camera.

We see that the discharge polarity has an influence on the appearance and structure of the dust layers. Typically, TREs with negative polarity create a macroscopically uniform dust layer, while TREs with positive polarity on the other hand lead to freckled dust layers with circular areas which appear to be denser and/or thicker. This leads to the expectation that dust layers will show different structures depending on the polarity of the corona. Therefore, in the following, SEM imaging was done in parallel for both polarities.

Figure 7b shows the SEM images of TRE #1 and TRE #2 at 100-fold magnification revealing even greater differences in dust layer structure. Experiments with negative polarity (e.g., TRE #2) tend to form μm -scale agglomerate-like protrusions. The protrusions are spread uniformly but appear to be aligned along the surface structures of the cold-rolled copper foil. For TREs with positive polarity (e.g., TRE #1, right side), a smooth dust layer is found with higher density circular areas (diameters 1–2 mm) as mentioned for visible light already. Furthermore, and apart from some dirt, the layers from positive corona

typically show some tiny white spots with diameters around 20 μm , which were identified as dendritic structures. These will be discussed later.

Figure 7c shows SEM images at 5000-fold magnification. For TRE #2 with negative polarity, we see a single protrusion of SiO_2 NPs which can still be identified. TRE #1 with positive polarity shows a part of the smooth surface with a dense uniform coverage with SiO_2 particles.

Figure 8 shows the dust layers from a lateral perspective after removing parts of the layer. With the negative corona, we observe a uniform layer of about 4 μm thickness and an originally smooth surface on which a large number of bigger and smaller protrusions has formed. Both the layer and the protrusions sitting on it appear to have comparable density and structure. The original, fractal structures of the SiO_2 aerosol nanoparticles are still visible. With the positive corona, the uniform dust layer is thicker (about 11 μm) and has a very smooth surface. By chance, none of the dendritic structures formed by positive corona is seen in the imaged section.

Figure 9 gives additional views from a lateral perspective showing the different structures of NP layers deposited with negative and positive corona, respectively. With negative corona, the rather smooth base layer is densely populated with agglomerate-like protrusions of variable size. The distance between the protrusions is comparable to their height. With positive corona, the NP layer thickness is extremely uniform, and the surface structure of the copper foil

substrate can be traced through the dust layer. Dendritic structures are scattered across the surface with distances ranging from 100 μm to several hundreds of μm . Compared to the size of the dendritic structures, the distances are quite big.

Figure 10 gives another lateral view showing more details. With negative corona, the agglomerate-like protrusions appear to be very fluffy. Especially from the top of the larger protrusions, fractal structures are extending into the free space.

In contrast, the density of the dendritic structures formed with positive corona is very high. In detail, the typical morphology is characterized by several cylindrical, unbranched arms originating from a central spot and stretching out radially. The dendritic structure itself is surrounded by an area where the dust layer structure is coarsened. It appears that the primary SiO_2 agglomerates have disappeared by a kind of sintering process. It appears that intensive discharges are taking place at the end of the longer dendrite arms, raising the temperature by several hundreds of degrees and leading to a fast sintering of the NPs. The coarsened structure observed around the primary dendrites (compare Fig. 10) appears to be a field of sintered SiO_2 developing into smaller, secondary dendrites. Most probably, the development of the secondary dendrites is induced by heat radiation or

heat conduction from the primary dendrites. During growth, the dendritic structure probably is enveloped into a plasma which is heated by an intensive, local gas discharge. It appears that the dendrites extend along the electrostatic field lines inside a (more or less) hemispherical plasma region. Obviously, a lot of material must be accumulated to form the dendritic structures.

Figure 11 (left) shows a detail from the tip of a dendrite arm grown in a TRE run with positive corona. It appears that the dendrite arms are hollow or highly porous. Hollow dendrite arms are found for all dendritic structures grown with positive corona. Hence, current could be transported through the dendrite arms either via conduction through the hot solid shell or via gas discharge in the hollow space.

Dense dendritic structures were mainly found with positive corona polarity. However, in some exceptional cases, sintered dendrites were also observed with negative corona. Figure 11 (right) shows one out of a few examples found on the sample from TRE #3. Interestingly, the dendrites formed with negative corona are not only much smaller, but also different in structure: The ends of these dendrite arms are always pointed, indicating that the arms should be massive.

The riddle on how dendrite formation is started still needs to be resolved. The SEM pictures give

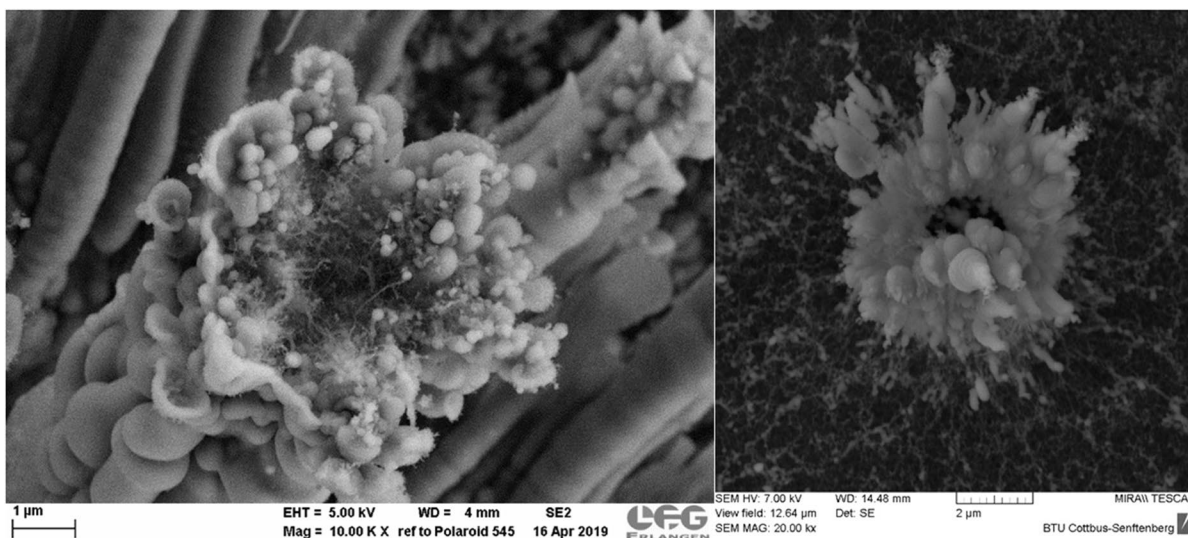


Fig. 11 SEM, different magnifications. The left image shows the commonly found end of a hollow dendritic arm, sample from TRE #4 with positive ESP polarity. The right image

shows a detailed view of a rare, sintered dendrite developed with neg. corona polarity (TRE #3)

two answers which are not necessarily compatible. In the case of the typical runs with positive corona, TRE #4/5, a few structures are found which may be interpreted as early, inhibited, or retarded stages of dendrite formation. Figure 12a (left) shows a typical example from TRE #4. We see a small irregularity of the dust layer from which small dendrites are emerging. The white spots observed on the TRE #1 sample (Fig. 7b, right) are similar in size, but do not show dendrites or any other sign of activity. Yet another answer on incipient dendrite formation might be derived from TRE #1, the first run in a brand-new collection electrode. This TRE was terminated about 20 min after the transition to the high current regime and to a high emission of

ICPs. But the large dendritic structures typical for the other runs with positive corona are not found on this sample, and the white spots visible in Fig. 7b (right) appear to be inactive. Instead, the dust layer shows tiny sunken-in spots which are spread on the surface at larger distance comparable to the dendrites from Fig. 9 (right). Figure 12b (left) shows a single sunken-in spot in the uniform dust layer. The sunken-in spots are approximately circular with a diameter of around 2 μm and are separated from the adjacent dust layer by a circular groove. In the central part, the NP layer has sintered to a visibly lower porosity. Figure 12b (right) shows the outer edge of the crater in larger magnification. Here we find still unsintered NP aggregates.

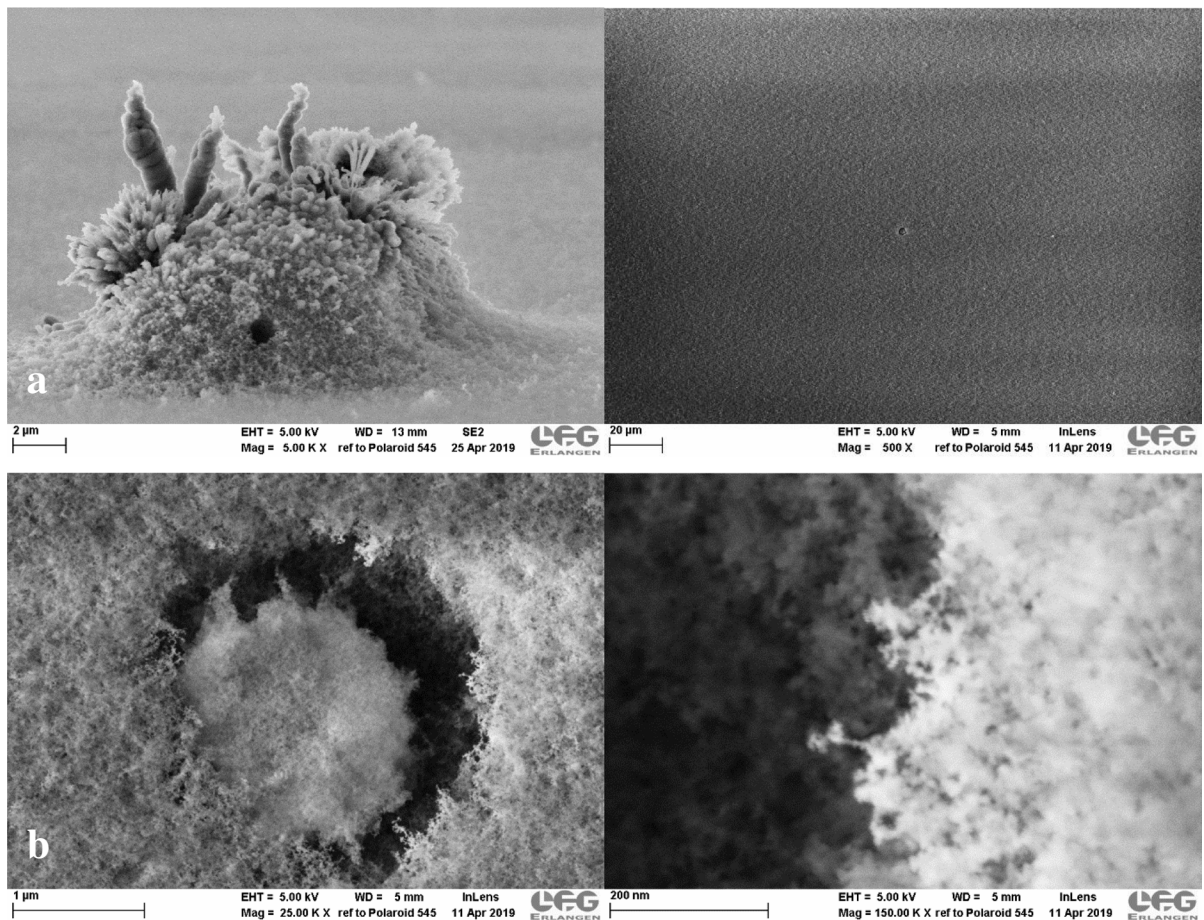


Fig. 12 SEM, different magnifications. **a** The left image shows a transient state of dendrite formation from TRE #4 with positive corona. The right image shows a disturbance in the smooth dust layer sample from TRE #1. **b** On the left

side, the disturbance is magnified and shows a sunken-in structure of higher density hinting at sintering processes. The right image shows a magnification at the edge of the crater

In order to investigate the suspected irreversible changes of the electrodes by the deposition of the NP layer, an intensified cleaning procedure (see Appendix) was applied to a dust sample from TRE #5 which then was reexamined by SEM. It was found that the dendritic structures withstand manual cleaning but some of the dendrite tips break off (see Fig. 13). The dust layer around the structure is removed to a large extent but a few layers of particles remain on the copper foil. Unfortunately, the original collection electrode was not available anymore at the time of the review. However, we do believe that cleaning was incomplete between the TRE runs, as less pressure was applied while wiping the surface of the collection electrode and sonication was not possible. However, it remains open to which extent the time-dependent changes are caused by remains of the dendrites or by the base layer of NPs remaining on the surfaces.

Summarizing, we have seen that the structure of the particle layers formed during BC strongly depends on the corona polarity.

The SiO₂ NP layers deposited by negative corona are macroscopically homogeneous. These layers consist of a thin homogeneous layer of SiO₂ agglomerates, which is covered by larger, densely spaced agglomerate-like protrusions with diameters ranging from 5 to 20 μm. The protrusions themselves have got a very high porosity.

SiO₂ NP layers deposited by positive corona are showing circular freckles with a higher packing density. The freckles are about 1 mm in diameter, but do not protrude from the surface. The surface of the layers is mostly smooth. Sintered dendritic structures with about 20 μm in diameter and in height are dispersed irregularly across the surface. The larger arms at the center of these structures are always hollow. The average distance between these structures may be estimated to be about 100–500 μm. The dendritic structures appear to be formed by sintered SiO₂. Occasionally, early (or aborted) stages of sintering, forming sunken-in circular spots of about 2 μm in diameter in the smooth dust layer, were observed.

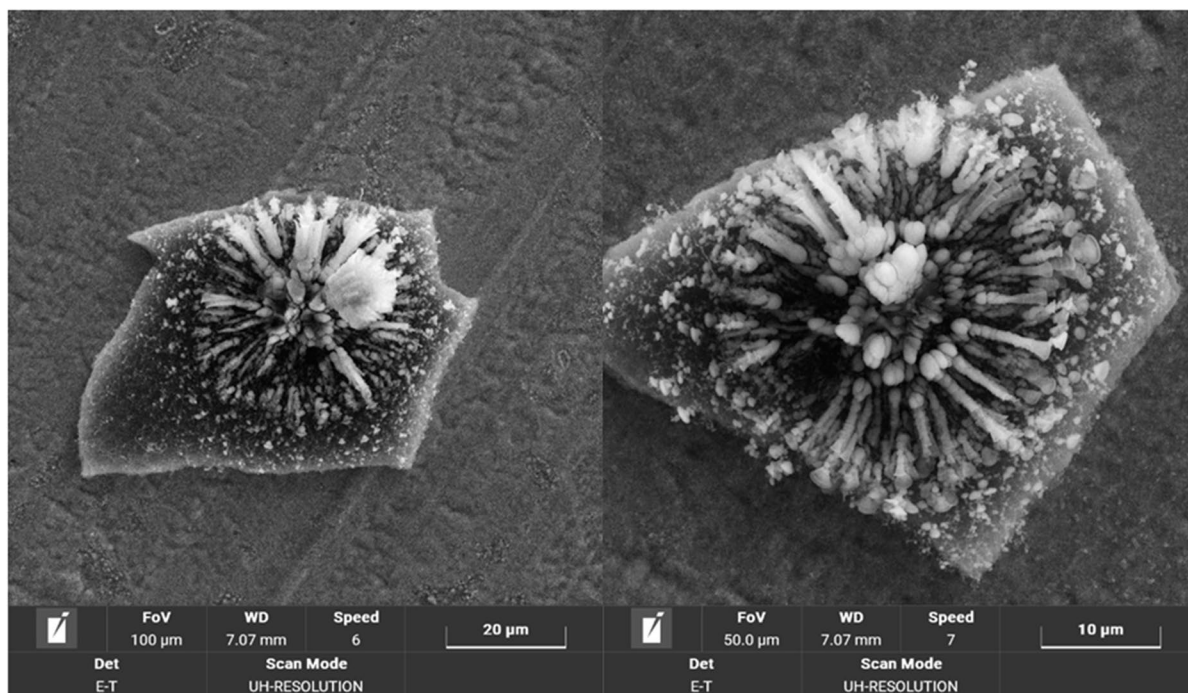


Fig. 13 SEM, different magnifications. Results of an intensified cleaning procedure applied to the sample of TRE #5 (positive polarity) showing partial removal of the dust layer and damaged dendritic structures. The dendritic structures

even protect the underlying dust layer from removal. Also, a thin base layer of SiO₂ NPs is remaining on the surface. Both effects can contribute to an irreversible change of the collection electrode

These distinct differences in dust layer structure are remarkable for comparable operation time and separation efficiency in both experiments. Hence, it is not surprising that polarity-dependent behavior is observed in the time-response experiments. Concluding from the structural differences, the BC mechanisms must differ fundamentally between both polarities. This will be in the focus of the following discussion.

Discussion

We have observed the emission of charges (by BC) from NP layers during the deposition of highly resistive SiO₂ NPs in an electrostatic precipitator operated at a moderate temperature of around 200 °C. While highly porous layers of SiO₂ NPs (porosity 90–95%) with a thickness of 4 to 11 μm were being deposited during 100 min, the current uptake of the ESP was rising very strongly (13- to 17-fold) above the low current level measured shortly after the admission of aerosol, and even much above the current measured without aerosol in the initial phase. Simultaneously, the separation efficiency dropped from near 99% down to about 30%.

The existence of BC was undoubtedly confirmed by the occurrence of large quantities of ICPs in the clean gas aerosol leaving the ESP. The TREs have shown that BC develops already within a short time (10 to 50 min) after starting the electrostatic deposition. Hence, BC starts already while the thickness of the NP layer is in a range of only 0.4 to about 5 μm.

With both corona polarities, the mechanism of BC appears to be different from “traditional” BC. Traditionally, the mechanism of BC is thought to be an electric breakthrough of the dust layer occurring at a certain critical field strength within the dust layer (Masuda et al. 1995). In experimental observations, traditional BC typically is associated with the formation of pores or craters in the dust layers, and with the formation of a gas discharge within the pores. The formation of pores or craters can be explained mechanistically from the interaction of the electrostatic field with the layered, bipolar space charge distribution within dielectric dust layers (Aleksin et al. 2016). Possibly local heating and melting of the dust layer could be another mechanism of pore formation.

Here, with highly resistive NPs, we observe a completely different mechanism of BC formation. In the first place, the dust layers are completely free from the macroscopic pores which usually are the sites of BC. Even though the particle layer does have a high porosity, the pores are very small, certainly far below 1 μm, due to the small primary particle (20 nm) and particle aggregate (170 nm) diameter. The primary particle diameter was estimated from SEM images of SiO₂ aggregates from the raw gas collected on a nuclepore filter (not shown here).

Remarkably, the electric field E within the NP layers is very strong. The experiments allow quantifying this at least roughly. Looking at a highly resolving presentation of the current uptake in the initial phase of the TRE runs (Fig. 3b), we find that the current uptake drops quite significantly during the first “falling current” phase of NP layer build-up. As the current uptake of a corona discharge is space charge limited, a decrease of current uptake exactly corresponds to a decrease of ionic space charge in the corona and to a decrease of potential drop in the corona process, as it is described by the CVC of the corona. On the other hand, the lower potential difference from the corona discharge must be compensated for by an increasing potential drop across the NP dust layer.

For the following estimate of E within the NP layer, we refer to the TRE #4 measurement, because it shows a typical behavior in the “falling current” phase, very much similar to the following TRE #5. For the time between $t_m = 11$ and 21 min, the current uptake goes back from 0.35 to 0.15 mA, which gives an average slope of $-20 \mu\text{A}/\text{min}$. During this period of time, the separation efficiency has remained on a high level (around 90%), and there were no signs of beginning charge emission from the NP layer. Notably, the emission of ICPs was on a low level. Now, the slope of the CVC at +10 kV/200 °C is $0.21 \mu\text{A}/\text{V}$ (see Fig. 6b, clean pipe, pos. corona). Based on this, an increase of voltage drop across the growing dust layer amounting to 95 V/min is derived from the current slope of $-20 \mu\text{A}/\text{min}$. From Fig. 8 (showing a NP layer of 11 μm formed between $t_m = 10$ and 110 min), we find that the time-averaged growth rate of the NP layer was $0.11 \mu\text{m}/\text{min}$. But we need to correct this value because the growth rate is higher in the beginning and lower in the end of the TRE runs, depending on the precipitation efficiency. For TRE #4, Fig. 5 shows a time-averaged separation efficiency of 48%

(determined by numerical integration), while the separation efficiency in the initial “falling current” phase was 95%. Hence, the separation efficiency and the growth rate in the initial “falling current” phase were higher by a factor of $0.95/0.48$, giving a corrected growth rate of $0.22 \mu\text{m}/\text{min}$. Finally, the ratio between voltage drop change and layer growth rate yields the electric field inside the growing layer as $E=432 \text{ V}/\mu\text{m}$ or $432 \text{ kV}/\text{mm}$. In a further step, with the averaged current density of $0.96 \text{ mA}/\text{m}^2$ (0.25 mA on a precipitation area of $A=0.259 \text{ m}^2$), we find the resistivity of the NP layer $\rho_{\text{el}} = E/i = EA/I$, where A is the precipitation area and I the current uptake. With the above values for TRE #4, $\rho_{\text{el}}=4.5\cdot 10^{13} \Omega\cdot\text{cm}$ is found for positive corona.

An analogous calculation for TRE #1 (with a current decrease slope of $-5 \mu\text{A}/\text{min}$ and an averaged current of 0.33 mA ($\cong 1.27 \text{ mA}/\text{m}^2$) in the time interval between 11 and 31 min) yields an electric field of $E=108 \text{ kV}/\text{mm}$ and a resistivity of $\rho_{\text{el}}=8.5\cdot 10^{12} \Omega\cdot\text{cm}$.

Of course, the above calculation can give a rough estimate only, because it neglects that NP layer thickness and current density are values which vary along the length of the collection electrode. Therefore, the resistivity value was confirmed by independent measurements in a standard set-up for dust resistivity measurement using a special NP layer sample produced during TRE #3. Here, the NPs were precipitated directly onto the electrode used in the resistivity measurements. As known from other situations, the resistivity of the NP layer depends on the current density, which is a fundamental property of current transport through dielectric materials (Aleksin et al. 2016). Values of $\rho_{\text{el}}=1.8\text{--}2.5\cdot 10^{13} \Omega\cdot\text{cm}$ for positive corona and of $\rho_{\text{el}}=1.6\cdot 10^{13} \Omega\cdot\text{cm}$ for negative corona were found with current densities between 2.2 and $3.0 \text{ mA}/\text{m}^2$ and electric fields of 440 to $550 \text{ kV}/\text{mm}$ were determined. For comparison, a volume resistivity in the order of $10^{13} \Omega\cdot\text{cm}$ is reported by Elmer and Nordberg (Elmer and Nordberg 1967) for bulk fused quartz at $200 \text{ }^\circ\text{C}$.

The above results show that extremely strong electric fields can build up during the formation of NP layers by electrostatic deposition. In comparison, the breakthrough field strength in air at $200 \text{ }^\circ\text{C}$ is around $1.85 \text{ kV}/\text{mm}$ only. The possibility of much stronger electric fields basically is explained by Paschen’s law for gas discharges in gaps between solid surfaces

(Paschen 1889; Raizer 1991). More recently, Paschen’s law has been modified by incorporating field emission or thermionic field emission into the theory (Go and Venkatraman 2014). The mechanism of thermionic field emission allows the emission of free electrons from a surface exposed to a strong electric field. While theory (Petrin 2009) predicts that thermionic field emission from ideal surfaces needs electric fields of $E\geq 10^9 \text{ V}/\text{m}$, real surfaces produce “appreciable current” already at $E=10^8 \text{ V}/\text{m}$ due to microscopic roughness (Raizer 1991).

Experimental investigations on current transport across narrow gaps between dielectric (glass) particles (Vora et al. 2019) have shown that self-sustaining or self-amplifying gas discharges cannot develop (in air at ambient pressure) with pore sizes below about $2 \mu\text{m}$. With dielectric materials, the supply of electrons is limited due to the high resistivity of the material. Meanwhile, thermionic field emission is strong enough to keep the field below the Paschen limit. This results in a continuous leak of current across the gap. For example, thermionic field emission with an averaged current density of $25 \text{ mA}/\text{m}^2$ was observed across a gap of $0.25 \mu\text{m}$ with an estimated field of $223 \text{ V}/\mu\text{m}$ (current 0.4 pA , particle diameter $145 \mu\text{m}$, particle projected area $16,500 \mu\text{m}^2=16\cdot 10^{-9} \text{ m}^2$, ambient temperature).

Other experiments by Ono et al. (2000) have shown a breakdown voltage of about 650 V for a $0.5\text{-}\mu\text{m}$ gap between Si electrodes (and still 350 V for a $5\text{-}\mu\text{m}$ gap), both for ambient temperature.

In the present case, we have to consider that the pores within the dust layer are well below $1 \mu\text{m}$. Interpreting the dust layer as a 3-dimensional, random assembly of Paschen gaps, we can understand that extremely strong electrostatic fields are possible in a layer of highly resistive submicron particles. Gas discharges cannot develop because the small pore diameters do not allow the multiplication of charge carriers by impact ionization in the gas. Excluding gas discharges, two possible mechanisms remain by which current can be transported through a porous NP layer:

First, the strong fields which were confirmed experimentally for the present NP layers allow the thermionic field emission of free electrons into the pore space from any surface within the dust layer. Further consequences from this will be discussed below. Second, in a parallel process, charge carriers

(electrons, holes) can be injected into the solid particles either from the side of the metal electrode or via gas ions from the corona discharge. The strong field and the elevated temperature help to overcome the work function for injection and reduce charge carrier immobilization due to the Poole–Frenkel-effect (Simmons 1967).

Electrons produced by thermionic field emission will move along the electric field lines until they collide either with a gas molecule or with a particle surface. The mean free path of electrons in air at 200 °C is estimated, using data from Raizer (1991), to be $\lambda_e = 0.7 \mu\text{m}$. The mean free path of electrons in a highly porous NP layer may be estimated using Lambert–Beer’s law in a formulation where particle concentration is expressed in terms of projected area (see (Riebel and Kräuter 1994)):

$$T = \exp\{-KC_{\text{PA}}\Delta z\} = \exp\left\{-K\frac{1.5}{d_p}C_V\Delta z\right\} \quad (2)$$

Here, T is the line-of-sight transmission of free electrons, K is the collision efficiency, C_{PA} is the projected area concentration, C_V is the volume concentration, d_p is the diameter of spherical particles, and Δz is the layer thickness or the free path of the electron. With $K=1$ (assuming hard-core collisions between electrons and NPs), the primary particle diameter $d_p=20 \text{ nm}$, and $C_V=0.05$, the median reach ($T=0.5$) of free electrons is estimated to be $\Delta z = 185 \text{ nm} = \lambda_{e,\text{NPL}}$. However, Lambert–Beer’s law applies to suspensions with freely moving particles, while the primary particles inside the NP layer are in direct contact with more than one particle. This leads to a mutual shading of the particles, and to a larger mean free path of the electrons. Furthermore, the particles are deposited as agglomerates with a median diameter of 170 nm. With a fractal dimension of 1.86 for agglomerates formed by aggregation (Schmid et al. 2004), the agglomerate porosity is estimated as 91.3%. Based on this approximation, “weak” zones with a higher porosity may exist between the agglomerates to reach the average layer porosity of 95%. Unfortunately, the current state of knowledge does not provide the basis for a quantitative calculation, but it seems realistic to estimate an overall electron mean free path in the range from $\lambda_{e,\text{NPL}} = 200$ to 250 nm.

The energy attained by electrons between two collisions with the NPs is $W = eE_{e,\text{NPL}}$. In our case with $E=108\text{--}432 \text{ V}/\mu\text{m}$, free electrons can reach an average electron energy ranging from $W=22$ to 108 eV. An energy of about 12 eV is already sufficient to produce secondary electrons by ionization of gas molecules (Raizer 1991). But the probability of gas-electron-collisions is not very high, as the mean free path of electrons in the gas is around $\lambda_{e,\text{gas}} = 700 \text{ nm}$ at 200 °C and hence about the three-fold of $\lambda_{e,\text{NPL}}$. On the other hand, an electron energy above about 40–60 eV is sufficient to obtain a secondary electron emission coefficient $\gamma_e > 1$ on glass and quartz surfaces (Raizer 1991).

Concluding, we see that in the pore space of the NP dust layer when subjected to a strong field, gas discharges are suppressed, but free electrons can be produced and probably multiplied comparable to a microchannel plate detector. In addition, electrons and holes can be transported via the solid phase.

Free electrons produced in the NP layer will enter into the gas phase when the corona polarity is positive. With data provided by Raizer (1991) for the characteristic time of electron attachment and electron mobility in air, with a correction for the temperature-dependent gas density and assuming an average electric field of 0.25 kV/mm, we find that the electrons will travel through a characteristic distance of about 460 μm before being converted into negative gas ions by attachment to electronegative gas molecules. Meanwhile, the energy of the electrons is dissipated much faster. The energy relaxation length Λ_w (Raizer 1991) is $\Lambda_w \cong 0.8 \lambda_e / \sqrt{\delta}$, whereby δ is the rate of momentum transfer per collision. For lower electron energies ($< 12 \text{ eV}$), collisions are mostly elastic and δ is in the range $\delta = 10^{-2}\text{--}10^{-3}$, leading to $\Lambda_w = 5\text{--}15 \mu\text{m}$. Electrons with higher energy have a much higher rate of momentum transfer, with inelastic collisions leading to the ionization or excitation of gas molecules. Hence, these processes occur in a very thin layer near the NP layer surface.

In the interface between the dust layer and the gas phase, different scenarios are possible. From the gas discharge, gas ions are travelling through the gas. With the mobility of the gas ions and the current density, a certain value of the electrostatic field in the gas is established. In the present experiment, the average field between wire and tube wall

is quite low (0.25 kV/mm). The space charge of an aerosol can lead to some increase of the field at the collection electrode (Robinson 1971; Lübbert 2011), but sparking generally prevents that average fields above 1 kV/mm (1 V/ μm) can be maintained. Hence, the field in the NP dust layer is about two orders of magnitude higher compared to the field in the gas phase. Relatively small inhomogeneities in the dust layer thickness or conductivity will lead to a significant distortion of the electric field in the boundary region.

Assuming a dust layer of uniform conductivity but inhomogeneous thickness, the electric field lines will be contracted towards the areas where the dust layer thickness is less. Particles being charged with the polarity of the corona will follow the field lines and will be deposited preferentially to areas where the dust layer is thinner. This explains, in the first place, why we find homogeneous dust layers with a smooth surface.

A destabilization of the dust layer thickness is possible in the case that the dust layer resistivity decreases significantly with increasing layer thickness. This occurs when the field within the dust layer is strong enough to produce secondary electron emission. In the case of $\gamma_e > 1$ in combination with a sufficient dust layer thickness s ($s \gg \lambda_e$), additional dust layer thickness will lead to a strong increase in the production of free electrons (departing into the pore space) and of holes (left behind in the solid phase). In addition, a thicker layer will allow a more efficient conversion of UV light into photoelectrons. Hence, we should expect a progressive decrease of resistivity with increasing layer thickness and a destabilization of the layer surface when a critical layer thickness has been surpassed.

Now, when the dust layer resistance is lower in areas with a higher layer thickness, the electric field lines will contract towards these areas. Ions and charged aerosol particles follow the field lines and will be deposited preferentially to these areas, locally producing a higher current density and a higher NP layer growth rate. The resistivity of dust layers generally goes through a maximum in the temperature range between 150 and 300 °C, which is explained by a transition from surface conduction (at lower temperatures) to volume conduction (at elevated temperatures) (White 1963, 1974). Hence, the negative temperature coefficient of dust or NP layer resistivity

at elevated temperatures can further contribute to the destabilization of the NP layer thickness, to a local accumulation of dust particles, and to a non-uniform layer structure. It appears that the sunken-in spots depicted in Fig. 12b correspond to this initial phase of local current concentration and heat production.

Different mechanisms of current transport in the interface between NP dust layer and gas phase can explain the different appearances and spacing of the surface structures in case of positive and negative corona.

Assuming a negative corona discharge, positive charge carriers (holes) will migrate from the electrode to the surface of the NP dust layer but are not able to leave the surface. In case that a sufficiently strong field is reached locally on a protrusion of the layer surface, a local gas discharge can be generated. Positive gas ions from the protrusion will spread into the gas and recombine with negative gas ions from the corona discharge. As positive and negative gas ions have similar values of mobility, positive ions spreading from one protrusion will attract negative gas ions from the corona discharge, influencing a region with a radius corresponding approximately to the height of the protrusion. While the protrusions are growing, less and less protrusions can coexist within a given area, and smaller protrusions cease to grow further. This corresponds to the pattern visible in Figs. 9 and 10 (left). Ions are collected from a rather small area only, and the local energy concentration is not sufficient to cause a sintering of the SiO₂ NPs.

Assuming a positive corona discharge, free electrons generated in the pore space simply can leave the pores. As discussed above, the free electrons will travel for a characteristic distance of about 460 μm before they are converted into negative gas ions. A competing process is the direct recombination with positive gas ions. However, compared to gas ions, the free electrons travel faster by a factor of about 300 to 400 and current is transported without producing a significant electron space charge. Applying Fermat's principle of shortest transport time to the situation of combined current transport by free electrons, negative and positive gas ions, we find that the electrons can spread widely (in the order of the characteristic electron distance of 460 μm) and neutralize the positive ions from a large area. Hence, much more current can be focused onto one emissive spot, which allows local heating until the sintering temperature of

SiO₂ is reached. This explains that the current emitting structures (sunken-in spots, dendrites) are pretty far apart in the case of positive corona. The distances between the dendrites in Fig. 9b (right) correspond quite nicely with this prediction.

With the sintering of SiO₂, the pores disappear. But due to the high temperature, SiO₂ is electrically conductive. Hot spots in the surface and even more so hot, quasi-conductive dendrite arms extending from the surface can trigger gas discharges by different mechanisms. Generally, the hot surface leads to a local heating of the gas. The local reduction of the gas density results in a lowering of the critical field strength which is necessary to start a self-sustaining gas discharge. Especially with positive corona discharges, the hot spots on the collection electrode can become sources for the emission of free electrons by thermionic emission or thermionic field emission.

Another scenario might be to assume that positive ions are emitted from the NP layer in case of negative corona discharges. Alkali metal cations might be emitted with rather low temperatures already (Peineke and Schmidt-Ott 2008). However, there is no mechanism known which might explain how an increased thickness of the NP layer might lead to an increased emission of cations. Hence, this scenario is neither able to explain the time behavior of negative BC nor the instability of the NP layer thickness which is developing with negative discharge polarity. On the other hand, the presence of alkali ions in the dust is known to reduce the resistivity and to prevent BC in case of sufficient concentration (White 1974).

Conclusion

The electrostatic precipitation of a flame-generated SiO₂ aerosol at 200 °C was investigated, whereby a SiO₂ nanoparticle (NP) layer with a thickness of a several μm was formed on the collection electrode.

Concerning the process of electrostatic precipitation, a high precipitation efficiency was found in the initial phase of the process, independently from the corona polarity. After deposition of a SiO₂ layer with critical thickness, a transition to back corona (BC) was observed. The first sign of incipient BC was a deterioration of the separation efficiency in all cases. With positive corona, this was observed

after 20 to 50 min of operation, corresponding to a layer thickness of 4 to 10 μm. With negative corona, this was observed after 2 to 10 min already, corresponding to a layer thickness of 0.4 to 2 μm approximately. As a second sign, an increase of the current uptake—generally seen as the classical indicator of BC—was found. The increase of current uptake occurred typically after about 15 min for the positive corona and after about 20 min for the negative corona, corresponding to a layer thickness of about 3 to 4 μm. The increase of current uptake continues for about 30 min with the positive corona and for about 60 min with the negative corona, until a stable level is reached. Simultaneously to the rise in current uptake, the emission of inversely charged particles increases by two orders of magnitude. With fully developed BC, the current amounts to the 13- to 17-fold of the clean gas current uptake, and around 10% of the particles emitted in the clean gas are inversely charged.

Concerning the SiO₂ NP layers formed by electrostatic precipitation, the porosity is estimated to be in a range of 90 to 95%. In the initial phase, smooth, homogeneous NP layers are deposited. More or less simultaneously with the increase of current uptake, charge-emitting structures start to develop on the surface of the NP layer. The morphology of the structures is completely different for positive and negative corona polarity, respectively. With negative corona, the charge-emitting structures are fluffy agglomerates of NPs with a height of up to about 20 μm. These structures are distributed on the surface quite uniformly, with the distances corresponding to the height. With positive corona, the charge-emitting structures have much larger distances, between 100 and 500 μm, and collect the current from a much larger area. In these structures, the NPs obviously have sintered to a denser structure. Two different types of charge-emitting structures are observed in the case of positive corona discharge: In one sample taken shortly after the initiation of BC, sunken-in spots with about 2 μm in diameter and signs of beginning sintering were found. The other samples from positive corona were taken after a longer period of operation with BC. Here, larger dendritic structures (20 to 50 μm in diameter) with strongly sintered, cylindrical hollow arms stretching away from a central point were found. The difference between the charge-emitting structures is explained by the

emission of positive ions in one case and of much more mobile electrons in the other case.

The drop of corona current in the initial phase of NP layer formation indicates a very high resistivity of the NP layer. The electrical data show that the SiO₂ NP layers have an extremely high value of resistivity (in the order of $\rho_{el}=10^{13} \Omega\cdot\text{cm}$). Based on experimental data, the electrical fields inside the NP layer are found to be in a range between $E=108$ and $432 \text{ V}/\mu\text{m}$. With fields of more than $100 \text{ V}/\mu\text{m}$ (10^8 V/m), free electrons can be emitted from the surfaces within the NP layer by thermionic field emission. Within the highly porous NP layer, free electrons can travel for a free distance of 200 to 250 μm (estimated median value) and attain a kinetic energy in the order of 20 to 110 eV. This allows a current multiplication within the NP layer by secondary electrons from solid surfaces and impact ionization with gas molecules.

The mechanism of BC in highly resistive NP layers is quite distinct from BC in layers of μm -sized particles. As the mean free path of the free electrons in the gas is significantly smaller compared the mean free path of the free electrons in the NP layer, the gas phase cannot produce an electric breakthrough within the NP layer. Instead, we assume that BC starts with the emission of free electrons by field emission. Initially, the current density of emission is distributed uniformly for a uniform layer thickness. Later, the process of secondary electron formation can destabilize the NP layer build-up by reducing the layer's electrical resistance when a critical layer thickness has been surpassed.

The new mechanism of BC or charge emission from a NP layer which is described here is bound to extremely high field strengths $E > 10^8 \text{ V/m}$ inside the NP layer, allowing the thermionic field emission (or field emission) of free electrons from the NP material. At the same time, gas discharges must be suppressed by pore diameters which are small in relation to the mean free path of the gas molecules. Assuming a typical current density of $i=10^{-4} \text{ A/m}^2$, a dust or NP layer resistivity above $10^{12} \Omega\cdot\text{cm}$ will be required to produce these effects. Hence, BC will not occur with more elevated temperatures. The upper temperature limit depends on the temperature-dependent volume resistivity of the particle material (White 1974). According to data from Elmer and Nordberg (Elmer and Nordberg 1967), the upper limit of sufficiently high resistivity for SiO₂ layers is expected

for temperatures around 250 to 300 °C. On the other hand, high resistivity and BC can be found with any lower temperatures, provided that the adsorption of humidity on the NPs is excluded. Hence, this may be the case in very dry gasses of any kind and also under low pressure or vacuum conditions.

Altogether, the experiment described here has shown very interesting and new properties of nanoparticle layers and, most probably, a new mechanism of BC formation. Based on the observed properties, layers of highly resistive NPs could be used as an ultrathin high-performance isolator which can be precipitated on any shape or form. Additionally, a NP layer subjected to sufficient electric fields may serve as an electron emitter or electron multiplier.

Admittedly, some of the interpretations of the experimental findings are still speculative. More systematic experiments will be needed to get more precise data.

Acknowledgements We would like to thank Prof. Sabine Weiß and Dr. Sebastian Bolz (Department of Metallurgy and Materials Engineering, BTU Cottbus-Senftenberg), and Prof. Wolfgang Peukert and Dipl.-Phys. Bettina Winzer (Institute of Particle Technology, FAU Erlangen-Nürnberg) for providing the SEM images. Thanks are due to Mrs. Angelika Striemann for doing the dust resistivity measurements as well as to Mr. Uwe Zernsdorf and Mr. Florian Schmalzer from the machine shop.

Author contribution The manuscript was written through contributions from both of the authors. All authors have given approval to the final version of the manuscript.

Funding Open Access funding enabled and organized by Projekt DEAL. The authors gratefully acknowledge the financial support for this project (EFRE-StaF 23035000) from the European Fund for Regional Development.

Availability of data and material The datasets generated and analyzed during the current study are available from the corresponding author on reasonable request.

Code availability Not applicable.

Compliance with ethical standards

Conflict of interest The authors declare no competing interests.

Abbreviations AN: Aerosol neutralizer; BC: Back corona; CVC: Current-voltage characteristic; ESP: Electrostatic precipitator; HMDSO: Hexamethyldisiloxane; HT-ESP: High-temperature electrostatic precipitator; HV: High voltage; ICP: Inversely charged particle; NP: Nanoparticle; PMD: Particle mobility distribution; PSD: Particle size distribution; SMPS:

Scanning mobility particle sizer; TNC: Total number concentration; TRE: Time-response experiment. Acknowledgements We would like to thank Prof. Sabine Weiß and Dr. Sebastian Bolz (Department of Metallurgy and Materials Engineering, BTU Cottbus-Senftenberg), and Prof. Wolfgang Peukert and Dipl.-Phys. Bettina Winzer (Institute of Particle Technology, FAU Erlangen-Nürnberg) for providing the SEM images. Thanks are due to Mrs. Angelika Striemann for doing the dust resistivity measurements as well as to Mr. Uwe Zernsdorf and Mr. Florian Schmalzer from the machine shop.

Appendix

This appendix highlights the experimental procedure used for the conduction of the time-response experiments (TREs), the measurement of the current–voltage characteristics (CVCs), and the intensified cleaning procedure to investigate irreversible changes of the collection electrode. The results obtained during the TREs (current, particle size distribution, inversely charged particles) are shown in Chapter 3. The measurements of the CVCs are shown in Chapter 4. The irreversible changes of the collection electrode are discussed in Chapter 5.

Experimental procedure for time-response experiments

The basic experimental settings were as follows:

- Propane flow to the burner: 54 L/h; heat input: 1.4 kW
- Aerosol volume flow: 7.6 m³/h at operation temperature, 4.7 m³/h at 20 °C (incl. humidity)
- Aerosol temperature at the entrance of the ESP section: around 210 °C at t_0 , 240 °C at t_{end}
- Residence time in the ESP section: around 2.5 s
- ESP voltage: The ESP voltage during operation was always set to ± 10 kV
- Aerosol data at ESP inlet (determined from measurements in the exhaust section, with ESP voltage set to “off”), undiluted: $1.54 \cdot 10^8$ cm⁻³ with a median number diameter of 170 nm

Prior to each time-response experiment (TRE), the ESP is taken apart, cleaned thoroughly (1st wiping with a dry tissue paper, 2nd wiping with a wet tissue paper, and 3rd wiping with another fresh wet, fuzz-free tissue cloth) and reassembled to ensure a common starting point. The procedure for each experiment is as

follows: After 40 min of preheating, the temperature in the ESP is roughly constant at 210 °C. The HV power supply (10 kV, either positive or negative polarity) is activated and the “measurement time” (t_m) starts to run. The current is recorded with one sample per second. At $t_m=0$ min, both SMPS devices begin to conduct measurements simultaneously. At $t_m=10$ min, the bypass towards the HMDSO saturation tank is opened and the SiO₂ aerosol is fed into the ESP. The experiment is continued for 30 to 130 min, until the current uptake of the ESP and the particle emissions from the ESP have reached a stable level. Then, the HV power supply to the ESP is switched off. Five minutes later, the samples for the raw gas measurements are extracted from the exhaust pipe and 4 consecutive SMPS measurements are made. Meanwhile, the temperature is measured in the entrance to the ESP to get the final temperature of the experiment. Finally, the aerosol production is switched off.

Experimental procedure for current–voltage characteristic measurements

During the first experiments (TRE #1 to TRE #4), the CVCs at operating temperature were measured directly after the time-response experiment. In every case, the polarity used during the experiment is measured first. The current is measured both with increasing voltage and decreasing voltage to spot any hysteresis effects. However, hysteresis effects have not been found. After both polarities have been measured, the burner is switched off and the ESP cools down. After at least 2 h, the ESP is at room temperature and the CVCs are measured again for both polarities.

Later in the experimental campaign (TRE #5 to TRE #7), additional measurements for the CVCs at operating temperature were conducted with a different procedure: On the day after a time-response experiment, the ESP (still containing the precipitated dust) is heated to 200 °C and the CVC is measured for the polarity used in the prior experiment. Afterwards the ESP is cooled down again to room temperature, the 20 °C CVC is measured. Then, after 5 h it is heated up again to 200 °C and the other polarity is measured. This procedure is designed to ensure that any remaining charge in the dust layer is removed.

Intensified cleaning procedure to investigate the irreversible electrode change

This procedure only applies to the results presented in Fig. 13. Cleaning of the dust layer samples is done with a tissue paper wetted with water + detergent. The sample surface is wiped repeatedly (3 times), applying a pressure in the order of 1 N/cm². After wiping, the sample is sonicated in desalinated water with added detergent for 5 min. The sample is sonicated again in fresh desalinated water for 1 min to remove loose parts of the layer and the detergent. Then, the residual water film is blown off with pressurized air.

Open Access This article is licensed under a Creative Commons Attribution 4.0 International License, which permits use, sharing, adaptation, distribution and reproduction in any medium or format, as long as you give appropriate credit to the original author(s) and the source, provide a link to the Creative Commons licence, and indicate if changes were made. The images or other third party material in this article are included in the article's Creative Commons licence, unless indicated otherwise in a credit line to the material. If material is not included in the article's Creative Commons licence and your intended use is not permitted by statutory regulation or exceeds the permitted use, you will need to obtain permission directly from the copyright holder. To view a copy of this licence, visit <http://creativecommons.org/licenses/by/4.0/>.

References

- Aleksin Y, Vora AL, Riebel U (2016) A new understanding of electric conduction in highly resistive dusts and bulk powders. *Powder Technol* 294:353–364. <https://doi.org/10.1016/j.powtec.2016.02.031>
- Bacchiega G, Gallimberti I, Arrondel V, Caraman N, Hamill M (2006) Back-corona model for prediction of ESP efficiency and voltage-current characteristics. ICESP X Conference Papers, Cairns, Queensland
- Bürger P, Riebel U (2020) Electrostatic charging and precipitation of nanoparticles in technical nitrogen: highly efficient diffusion charging by hot free electrons. *J Aerosol Sci* 141:105495. <https://doi.org/10.1016/j.jaerosci.2019.105495>
- Chang C-L, Bai H (1999) An experimental study on the performance of a single discharge wire-plate electrostatic precipitator with back corona. *J Aerosol Sci* 30:325–340. [https://doi.org/10.1016/S0021-8502\(98\)00064-0](https://doi.org/10.1016/S0021-8502(98)00064-0)
- Elmer TH, Nordberg ME (1967) Effect of nitriding on electrolysis and devitrification of high-silica glasses. *J Am Ceram Soc* 50:275–279. <https://doi.org/10.1111/j.1151-2916.1967.tb15108.x>
- Go DB, Venkatraman A (2014) Microscale gas breakdown: ion-enhanced field emission and the modified Paschen's curve. *J Phys D Appl Phys* 47:503001. <https://doi.org/10.1088/0022-3727/47/50/503001>
- Hoferer B, Schwab AJ (2000) Local occurrence of back corona at the dust layer of electrostatic precipitators. In: 2000 Annual Report Conference on Electrical Insulation and Dielectric Phenomena. IEEE, Piscataway, pp 93–96
- IFA (2019) GESTIS substance database - hexamethyldisiloxane. http://gestis-en.itrust.de/nxt/gateway.dll/gestis_en/003210.xml?f=templates&fn=default.htm. Accessed 03 Jan 2020
- Jánský J, Bessières D, Paillol J, Lemont F (2014a) Numerical simulation of transitions between back discharge regimes. *Eur Phys J Appl Phys* 68:20801. <https://doi.org/10.1051/epjap/2014140223>
- Jánský J, Gaychet S, Bessières D, Soulem N, Paillol J, Lemont F (2014b) Numerical simulation of back discharge ignition. *J Phys D Appl Phys* 47:65202. <https://doi.org/10.1088/0022-3727/47/6/065202>
- Lawless PA, Sparks LE (1980) A mathematical model for calculating effects of back corona in wire-duct electrostatic precipitators. *J Appl Phys* 51:242–256. <https://doi.org/10.1063/1.327416>
- Lübbert C (2011) Zur Charakterisierung des gequenchten Zustandes im Elektroabscheider. Dissertation, BTU Cottbus
- Majid M, Wiggers H, Walzel P (2011) Dust resistivity measurement and onset of back corona in electrostatic precipitators. *I J Pest* 5:185–190. <https://doi.org/10.34343/ijpest.2011.05.02.185>
- Masuda S, Hosokawa S (1995) Electrostatic precipitation. In: Chang J-S, Kelly AJ, Crowley JM (eds) Handbook of electrostatic processes. Marcel Dekker Inc, New York, pp 441–480
- Monrolin N, Praud O, Plouraboué F (2018) Revisiting the positive DC corona discharge theory: beyond Peek's and Townsend's law. *Phys Plasmas* 25:63503. <https://doi.org/10.1063/1.5031780>
- Ni M, Yang G, Wang S, Wang X, Xiao G, Zheng C, Gao X, Luo Z, Cen K (2016) Experimental investigation on the characteristics of ash layers in a high-temperature wire-cylinder electrostatic precipitator. *Sep Purif Technol* 159:135–146. <https://doi.org/10.1016/j.seppur.2016.01.011>
- Ono T, Sim DY, Esashi M (2000) Micro-discharge and electric breakdown in a micro-gap. *J Micromech Microeng* 10:445–451. <https://doi.org/10.1088/0960-1317/10/3/321>
- Paschen F (1889) Ueber die zum Funkenübergang in Luft, Wasserstoff und Kohlensäure bei verschiedenen Drucken erforderliche Potentialdifferenz. *Ann Phys* 273:69–96. <https://doi.org/10.1002/andp.18892730505>
- Peineke C, Schmidt-Ott A (2008) Explanation of charged nanoparticle production from hot surfaces. *J Aerosol Sci* 39:244–252. <https://doi.org/10.1016/j.jaerosci.2007.12.004>
- Petrin AB (2009) Thermionic field emission of electrons from metals and explosive electron emission from micropoints. *J Exp Theory Phys* 109:314–321. <https://doi.org/10.1134/S1063776109080184>

- Raizer YP (1991) Gas discharge physics. Springer-Verlag, Berlin Heidelberg
- Riebel U, Kräuter U (1994) Extinction of radiations in sterically interacting systems of monodisperse spheres. Part 1: Theory. Part Part Syst Charact 11:212–221. <https://doi.org/10.1002/ppsc.19940110308>
- Robinson M (1971) Electrostatic precipitation. In: Strauss W (ed) Air pollution control: part I. Wiley-Interscience, Wiley, New York, pp 227–335
- Schmid H-J, Tejwani S, Artelt C, Peukert W (2004) Monte Carlo simulation of aggregate morphology for simultaneous coagulation and sintering. J Nanopart Res 6:613–626. <https://doi.org/10.1007/s11051-004-2161-x>
- Seipenbusch M, Rothenbacher S, Kirchhoff M, Schmid H-J, Kasper G, Weber AP (2010) Interparticle forces in silica nanoparticle agglomerates. J Nanopart Res 12:2037–2044. <https://doi.org/10.1007/s11051-009-9760-5>
- Simm W (1959) Untersuchungen über das Rücksprühen bei der elektrischen Staubabscheidung. Chem Ing Tec 31:43–49. <https://doi.org/10.1002/cite.330310110>
- Simmons JG (1967) Poole-Frenkel effect and Schottky effect in metal-insulator-metal systems. Phys Rev 155:657–660. <https://doi.org/10.1103/PhysRev.155.657>
- Townsend JS, Edmunds PJ (1914) LXXXIX. The discharge of electricity from cylinders and points. Philos Mag 161:789–801
- Vora AL, Stepputat J, Riebel U (2019) Force and current in a contact gap between single highly resistive particles: experimental observations. J Phys Commun 3:95001. <https://doi.org/10.1088/2399-6528/ab3e2b>
- White HJ (1963) Industrial electrostatic precipitation. Addison-Wesley Publishing Company Inc, Reading
- White HJ (1974) Resistivity problems in electrostatic precipitation. J Air Pollut Control Assoc 24:313–338. <https://doi.org/10.1080/00022470.1974.10469923>

Publisher's note Springer Nature remains neutral with regard to jurisdictional claims in published maps and institutional affiliations.